*Journal of Fluorescence, Vol. 12, Nos. 3/4, December 2002 (© 2002)*

# 1 and 2-Photon Fluorescence Anisotropy Decay to Probe the Kinetic and Structural Evolution of Sol-Gel Glasses: A Summary

**Chris D. Geddes**[1]

*Received May 6, 2002; accepted June 12, 2002*

We review recent 1- and 2-photon fluorescence studies of the formation dynamics and structure of sol-gel glasses, from nanometre-sized particles to clusters, prepared from both aqueous silicates and tetramethylorthosilicate (TMOS), over a broad pH range. Through the careful choice of a fluorescent probe, anisotropy decay has been shown to provide both silica particle size and viscosity information and offers advantages over traditional techniques for silica particle sizing based on small-angle neutron, Xray, or light scattering. Subsequently, we are now able to observe the self-assembly mechanisms (or recently termed *kinetic life history*) of silica, produced under both acidic and alkaline conditions from sodium silicate solution (water glass) in the case of hydrogels and from alkoxides in the case of alcogels. The controlled preparation of hydrogels, often deemed a blackart, is also discussed in some detail, as are the potential applications and benefits of fluorescence anisotropy decay to industrial sol-gel systems. The insight into the sol-gel process provided by these new interpretations of fluorescence decay data, promises to have implications for both our fundamental understanding and the production of sol-gel systems in general.

**KEY WORDS:** Fluorescence anisotropy; sol-gel; silica hydrogel; silicon alkoxide; LUDOX colloidal silica; silica nanoparticles; reaction limited cluster aggregation; diffusion limited cluster aggregation; self-assembled nanoparticles.

## INTRODUCTION

The sol-gel process allows the preparation of room temperature oxide glasses, involving a series of hydrolysis and condensation steps to produce a rigid network, after a time denoted $t_g$, (the gelation time), which owes its origins to the pioneering work of Ebelman, Mendeleyev, and Graham in the nineteenth century [1]. The gelation time marks the onset of the gel and $t_g$ is strongly pH and temperature and silica concentration dependent. Prior to $t_g$ ramified nanometer size clusters of silica form and diffuse. Eventually this process leads to the rigid network appearing at $t_g$, and other processes start to dominate as the solvent evaporates, pores form as the particles aggregate, condensation occurs, and the gel shrinks (syneresis) and ages. After formation the gel can be strengthened; the surface area can be specified by a process called aging and is then typically dried to produce either a xerogel or an aerogel [1,2]. To produce stable non-changeable monoliths, as is the case in sol-gel optics and photonic devices, drying control chemical agents are added and the sol-gels densified [1,2]. These important and complex transformations constitute the life history or kinetic evolution of a sol-gel.

Controlling the reactivity of monomers used in

[1] Department of Physics and Applied Physics, University of Strathclyde, 107 Rottenrow, Glasgow, G4 ONG, Scotland, UK. *Current mailing address*: Institute of Fluorescence, University of Maryland Biotechnology Institute, and Center for Fluorescence Spectroscopy, University of Maryland School of Medicine, Medical Biotechnology Center, 725 West Lombard Street, Baltimore, 21201, MD. e-mail: Chris@cfs.umbi.umd.edu



1053-0509/02/1200-0343/0 © 2002 Plenum Publishing Corporation

the sol-gel process is chemistry whilst controlling the physical properties of sol-gel polymers in respect of size, structure, growth, porosity, density, etc. is physics. Although the chemistry is in general well understood, the complexity of the physics can be gauged from the fact that many of the chemical processes occur simultaneously, not sequentially, although at different times, different reaction rates may dominate. For example, for a while, even after $t_g$, most of the volume is still a liquid. Control of the polymerization produces a wide range of materials. These include stable colloids of well-defined nanoparticles, for example, Dupont's Ludox (which has many uses, although it is known in the field of fluorescence as a light-scattering medium for recording excitation pulse profiles), optical quality components used in photonics, porous glasses used in sensors, and the ubiquitous uses of silica gel powder.

A clearer picture of how controlling the competitive rates in the sol in the very early stages translate into the final gel is not only important to our fundamental understanding, but also in optimizing manufacturing processes. The link between particle size in the sol and pore size in the gel is a classic example, which spans the whole kinetic evolution of silica gel. Of course any technique for monitoring such changes should ideally be capable of monitoring *in situ* the whole process through to completion. Fluorescence is *par excellence* a method of determining reaction rates and, although ideally suited to the task in sol-gels, its capabilities have perhaps been hitherto under-appreciated in this context.

Traditionally, small-angle scattering of laser light, x rays, or neutrons has been used to study silica particle growth. For example, light scattering measurements found a primary particle hydrodynamic diameter of 1.0 nm, increasing to 2.4 nm prior to gelation [3]. Small-angle x-ray scattering studies of silica gel have revealed evidence for 1-nm particles [4], and similar studies on a silica sol indicate that 2-nm-diameter primary particles aggregate to form secondary particles of 6-nm-diameter before gelation [5]. Small-angle neutron scattering has found comparable primary particle dimensions [6]. However, scattering methods have a number of drawbacks. For example, they need low silicate concentrations to avoid multiple scattering, and dilution is not the answer, because it can cause depolymerization. Moreover, scattering by the gel matrix after $t_g$ corrupts the particle scattering measurement. X-ray and neutron scattering in particular are also very expensive and unsuitable for on-line use. Light scattering is limited in resolution by the wavelength of light, and electron microscopy can only be used on dry colloids.

Fluorescence correlation spectroscopy [7] and fluorescence recovery after photobleaching [8] possess sufficient resolution for silica particle metrology, but also suffer from the need to dilute the sols and have the added complication of requiring a microscope.

Fluorescence probe spectroscopy has become an established tool for probing structure and dynamics at the molecular level [9] and has been used extensively for this purpose in the study of sol-gels [10]. In particular, fluorescence depolarization resulting from Brownian rotation of a molecular probe reports on the local mobility of the probe. Expressed most usually as an anisotropy function, both steady-state and time-resolved, the changes observed during alkoxide sol-gel polymerization have been interpreted by many solely in terms of viscosity [11–14] from initial mixing to well beyond the sol to gel transition after a time $t_g$. For example, Narang and co-workers [13] used phase-modulation fluorometry to study rhodamine 6G (R6G) in TMOS gels at a sol pH of 4, 6, and 8 and observed two anisotropy decay components from the outset to beyond $t_g$. These they attributed to the presence of two discrete microdomains of different viscosity. One viscosity of $\approx$2 cP remained more or less constant during polymerization and was associated with free R6G, and the other increased during polymerization to a value over an order of magnitude greater than the bulk or microviscosity even before $t_g$. This is perhaps a surprising result, because such a large microviscosity disparity might be expected to lead to phase separation, which was not reported (Fig. 1A).

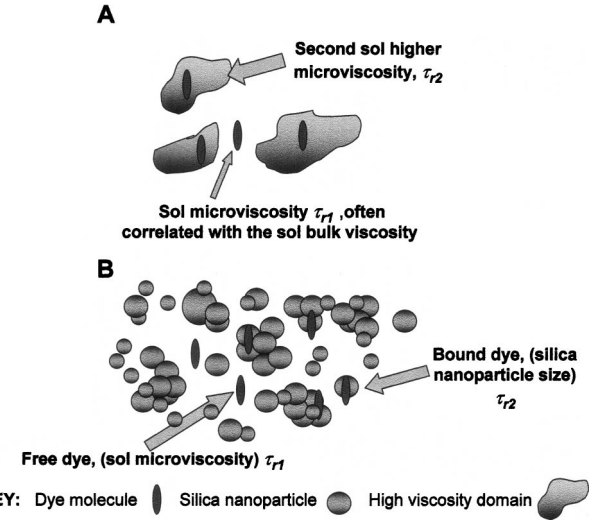


**Fig. 1.** (A) The fluorescent probe located in different viscosity domains (B) the probe partitioned between the aqueous phase and bound to growing (or aggregating) silica nanoclusters. $\tau_{r1}$ and $\tau_{r2}$ are the rotational correlation times from Eq. (10). From Geddes *et al.* [26].

In this review article we summarize our use of fluorescence anisotropy decay to determine the growth in the hydrodynamic radius of silica particles [15–26] Fig. 1B. Although fluorescence anisotropy decay has been widely used in biochemistry to determine structure and dynamics in membranes and proteins [27] it has hitherto found little if any application where the hydrodynamic radius of the fluorescing rotor species changes continuously with time. And yet fluorescence anisotropy decay is ideally suited to particle metrology during sol-gel polymerization, overcoming many of the drawbacks of scattering methods. For example, because in the absence of energy migration fluorescence anisotropy will decay only by rotating particles, growth can be studied at higher silicate concentrations than other techniques and even after gelation has occurred. Interestingly, although fluorescence has been widely used to study the sol to gel transition, the interpretation was for a long time confined to viscosity [10–14]. However, it has recently been shown [17,18] that the observed second and longer rotational correlation time can correspond to dye bound to particles (Fig. 1B), which has subsequently bridged the gap between scattering and fluorescence techniques and is providing new insight into silica growth mechanisms.

Evidence for the presence of growing silica nanoparticles in sol-gels is overwhelming from electron microscopy, neutron, X ray, and light scattering measurements, which have been performed on many different sol compositions in many different laboratories around the world. Our interpretation of fluorescence anisotropy data for doped sols reconciles the findings of fluorescence with those of these other techniques and offers a new approach to studying the dynamics and structure of sol-gel glass formation.

## SOL-GEL CHEMISTRY

The sol-gel process involves the transformation of a liquid-like solution, the sol, to, the gel, a highly porous matrix filled with solvent, through a series of hydrolysis and polycondensation steps. In the simplest case, the gel-forming step can be given by:

$$n\mathrm{Si(OR)_4} + 2n\mathrm{H_2O} \rightarrow n\mathrm{SiO_2}\ \text{(a growing gel network)} + 4n\mathrm{ROH} \quad (1)$$

where *R* can be either hydrogen for the case of hydrogels (an inorganic polymerization) or methyl, ethyl, propyl, etc. (an organic polymerization) for the case of alcogels, both so named in accordance with both the solvents used and condensed. The rates of formation and properties of the final gels derived from these organic and inorganic polymerizations are strongly pH, temperature, solvent, and $SiO_2$ concentration dependent [1,2]. There are many similarities between both processes and similar end-products are obtained. The alkoxide "alcogel" route is the one that has been mostly used for research into sol-gel processes because it has better defined reactants and is typically simpler to prepare than a hydrogel; the lower cost of the latter makes it ideal for industrial applications requiring mass production.

For hydrogels at pH $<2$ (acid catalyzed), gelation occurs by a means of a series of monomer and/or intercluster condensation reactions between silanol (Si-OH) bonds to form ramified siloxane type (Si-O-Si) clusters. For hydrogels polymerized from sodium silicate solution (water glass), a ternary system of $SiO_2$, $Na_2O$, and $H_2O$, then the gel forming step can be crudely described by:

$$\mathrm{Na_2O}.x\,\mathrm{SiO_2}.Y\mathrm{H_2O}\ \text{(water glass)} + \mathrm{H_2SO_4} \rightarrow \mathrm{SiO_2} + \mathrm{Na_2SO_4} + (Y+1)\mathrm{H_2O} \quad (2)$$

where *x* denotes the weight ratio (w/w) of the glass, that is, $SiO_2$:$Na_2O$, which for the work described here is $\approx 3.3$. It should be noted that the molar and weight ratio are almost equivalent, given that the relative atomic mass of $Na_2O$ and $SiO_2$ are 62 and 60, respectively. At a sol pH $<2$, the gel times are typically quite long where the polymerization rate is thought to be proportional to $[H^+]$ and the silicate species are thought to be positively charged but not highly ionised [1]. Also in the absence of the fluoride ion, the solubility of silica below pH 2 is quite low, except at very high proton concentrations. It is therefore likely [2] that the formation and aggregation of primary particles occurs rapidly together and that Ostwald ripening (a process whereby particles grow in size but decrease in number as highly soluble small particles dissolve and reprecipitate on larger, less soluble nuclei), contributes little to particle growth after the particles exceed 1 nm radius. Therefore gels polymerized at $<$pH 2 are thought to be composed of very small particles indeed.

At intermediate sol pH of 2–7, the gel times steadily decrease and it is therefore thought that above the isoelectric point the condensation rate is proportional to [OH] as shown below [1,2].

$$\equiv\mathrm{Si-OH} + \mathrm{OH^-} \rightarrow \equiv\mathrm{Si-O^-} + \mathrm{H_2O}\quad \text{(Fast process)} \quad (3)$$

$$\equiv\mathrm{Si-O^-} + \mathrm{HO-Si} \rightarrow \equiv\mathrm{Si-O-Si}\equiv + \mathrm{OH}\quad \text{(Slower process)} \quad (4)$$

In silicate species, the most acidic silanols (those which are most readily deprotonated) are those contained in the most highly condensed species. Therefore condensation (Eq. 4), occurs preferentially between more highly condensed species and less highly condensed, neutral species. Subsequently, the rate of dimerization is low, but, once formed, dimers will react preferentially with monomer to/from trimers and so on. This leads to the cyclization of species, because of the close proximity of the silanol chain ends and subsequently the formation of the primary silica particles. The further addition of low molecular weight species to more highly condensed species rapidly depletes the monomer population. Further growth therefore occurs by aggregation or chaining to form the growing $SiO_2$ network.

At a pH above 7, hydrogel sol polymerization occurs by the same nucleophilic mechanism as for sols in the pH range 2–7 [Eqs (3) and (4)]. However, because all condensed species are likely to be negatively charged (highly ionized) and therefore mutually repulsive, growth occurs primarily by the addition of monomers to more highly condensed particles rather than by particle aggregation. Particles ≈1 nm radius are typically formed within minutes above pH 7. However, the presence of salts, which disrupts the silica particle surface charge, significantly reduces gel times, denoted a time $t_g$. Because of the greater solubility of silica and the greater size dependence of solubility above pH 7, the growth of primary particles continues by Oswald ripening. At a given pH, particles grow to a size that depends mainly on the temperature and $SiO_2$ concentration, where the growth rate depends on the particle size distribution.

At a much higher sol pH, $> \approx$ pH 12, most silanol groups are deprotonated and the primary building blocks are composed primarily of cyclic trimers and tetramers. Cyclic trimers are stable in this pH range because the somewhat planar, cyclic conformation permits the greatest separation of charge between the deprotonated sites.

Due to lack of salt and the mutually repulsive nature of the silica particles, stable, fairly high pH, non-gelling sols can be readily prepared or purchased [1]. In our work we have used one from DuPont's colloidal silica range, namely AM30, to investigate our approach to nanometre particle metrology on particles of known radius. Ludox AM30 silica particles are discrete, uniform spheres of amorphous silica with no internal surface area or detectable crystallinity. These 6-nm radius particles are dispersed in a pH 8.9 alkaline medium (NaOH), which reacts with the silica surface to produce a negative surface charge (deprotonated silanol groups), charge balanced with sodium ions. This is in fact similar to what is envisaged for hydrogels prepared from sodium silicate solution at a similar sol pH, but in the absence of destabilizing salts. In addition, some of the surface Ludox silica atoms have been replaced with aluminium atoms, which creates a fixed negative charge, independent of pH, affording particle stability over the alkaline range. This is a particularly important choice for the work described here, as water loss resulting from evaporation or slight changes in pH due to dissolved $CO_2$ has the potential to prematurely alter sol stability.

The alkoxide "alcogel" route, which is similar in many respects to the polymerization of aqueous silicates, can be described at the functional group level by three simple reactions [1]:

$$Si(OR)_4 + nH_2O \leftrightarrow Si(OR)_{4-n}(OH)_n + nROH$$

Hydrolysis (5)

$$\equiv Si-OR + HO-Si\equiv \leftrightarrow \equiv Si-O-Si\equiv + ROH$$

Alcohol Condensation (6)

$$\equiv Si-OH + HO-Si\equiv \leftrightarrow \equiv Si-O-Si\equiv + H_2O$$

Water Condensation (7)

and overall in the case of tetramethylorthosilicate (TMOS) by the net reaction:

$$nSi(OCH_3)_4 + 2nH_2O \rightarrow nSiO_2 + 4nCH_3OH$$

Net Reaction (8)

where R can be methyl, ethyl, or propyl groups, etc. The hydrolysis reaction (Eq. 5) effectively replaces alkoxide groups with hydroxyl groups, which can then readily condense to produce either water (Eq. 7) or alcohol (Eq. 6), where both reactions result in siloxane (Si-O-Si) bonds. Because of the fact that water and alkoxides are immiscible, a mutual solvent is typically used as a homogenizing agent, for example, an alcohol. As indicated by Eqs. 5 and 6, alcohol is not just a solvent but can participate in the reverse esterification and alcoholysis reactions respectively. The hydrolysis scheme (eq. 5) is generally acid or base catalyzed where the rate and nature of polymerization is pH dependent [1]. Other parameters such as temperature, pressure, the type of alcohol used, and the molar $H_2O$:Si ratio (sometimes denoted R:1) significantly influence the properties of the final gel [1]. It is widely accepted [1] that acid-catalyzed hydrolysis of a tetrafunctional alkoxide with low R values (typically $<2$) produces weakly branched *polymeric* type sols, whereas base-catalyzed hydrolysis with large R values produces highly condensed *particulate* sols. Intermediate conditions produce intermediate structures that lie within these boundary conditions [1].

Even after $t_g$, particles continue to play a role but new processes now start to occur as well, such as further condensation, dissolution, and redeposition.

## THEORY

Vertically and horizontally polarized fluorescence decay curves, $F_V(t)$ and $F_H(t)$, orthogonal to pulsed and vertically polarized excitation recorded at different delay times following initial mixing of the sol lead to an anisotropy function *R(t)* describing the rotational correlation function [9] where:

$$R(t) = \frac{F_V(t) - F_H(t)}{F_V(t) + 2F_H(t)} \tag{9}$$

If continuous excitation is used, the time-dependencies remain unresolved and a weighted average of the time-resolved anisotropies is observed in a multicomponent system such as a sol-gel to give a steady-state anisotropy *R*.

Our analysis for silica hydrogels and silicon alkoxides (TMOS), and also that of Narang and co-workers [13] on TMOS, showed that the best description of $R(t)$ was provided by two rotational correlation times $\tau_{r1}$ and $\tau_{r2}$ in the form:

$$R(t) = (1 - f)\, R_0\, exp(-t/\tau_{r1}) + fR_0\, exp(-t/\tau_{r2}) \tag{10}$$

where $R_0$ is the initial anisotrophy (Fig. 1). We interpret $f$ as the fraction of fluorescence due to probe molecules bound to silica particles and hence $1 - f$ the fraction due to free dye in the sol. From the Stokes-Einstein relation, $\tau_{r1}$ gives the sol microviscosity $\eta_1 = 3\tau_{r1}kT/4\pi r^3$, where $r$ is the hydrodynamic radius of the dye and likewise using $\eta_1$ and $\tau_{r2}$, gives the average silica particle hydrodynamic radius (Fig. 1B).

By expanding $\exp(-t/\tau_{r2})$ and putting $\tau_{r1} \ll \tau_{r2}$, to reflect the unbound probe molecules rotating much faster than those bound to silica particles, in the case in which the fluorescence lifetime $\tau_f \ll \tau_{r2}$, a similar expression to that encountered for the hindered rotation of a fluorophore in a membrane or protein [9] can be expected to hold in a sol-gel, that is, a residual anisotropy, $R_\infty$, is observed:

$$R(t) = (1 - f)\, R_0 \exp(-t/\tau_{r1}) + fR_0 \tag{11}$$

where $fR_0 = R_\infty$. If a fraction of the fluorescence, g′, is attributed to dye bound rigidly within the gel after $t_g$, as well as both free solvated dye and dye bound to silica particles then, if appropriate, Eq. 10 could be further extended to:

$$R(t) = (1 - f - g)\, R_0 \exp(-t/\tau_{r1}) + fR_0 \exp(-t/\tau_{r2}) + gR_0 \tag{12}$$

However in all our work, over many different types and sol compositions, Eq. 12, was not found to provide a good description of the anisotropy decays. Visually the anisotropy was observed to decay at all but the later polymerization times, suggesting that $g$ is a small fraction of the total fluorescence. However, one goal in our sol-gel studies was to use the shortest measurement time possible so as not to average out the size of the growing silica nanoparticles. Subsequently, it is likely that Eq. [12], although very plausible, cannot be supported by the statistical precision available for 1-photon excitation. Interestingly, using 2-photon excitation, the best description of anisotropy decay was also Eq. (10), where $g$ was found to be very small.

### Two-Photon Excitation

A multiphoton process originates when a molecule is excited to a higher electronic state by absorbing two or more photons in the same quantum event. In multiphoton excitation the fluorescence intensity, $I_{fl}$, does not increase proportionately with increasing excitation power density, $\rho_{exc}$, but follows the relationship:

$$I_{fl} = \gamma\, (\phi_{fl}/i)\, nd\, \sigma_i\, \rho^i \tag{13}$$

where $\gamma$ is a fluorescence collection efficiency factor, $\phi_{fl}/i$ the 1-photon excited fluorescence quantum yield corrected for the multiphoton absorption, $n$ the number density of absorber, $\sigma_i$ the absorption cross section for $i$ photons, and $d$ the sample path length. Equation 13 shows that in principle the gradient of a simple log-log plot of experimentally measured $I_{fl}$ and $\rho$ values allows $i$, the number of photons absorbed, to be determined.

One important difference with polarized multiphoton excitation, compared to our 1-photon studies, concerns the higher degree of molecular orientation photoselected and associated increase in the initial value of the fluorescence anisotropy ($R_0$). For multiphoton excitation a higher degree of orientation of molecules is required at $t = 0$ according to a directional distribution function $f_i(\theta)$, which can be approximated for the case of cylindrical symmetry and a dominant transition tensor to be [28]:

$$f_i(\theta) = cos^{2i}\, \theta \tag{14}$$

where $\theta$ is the angle between the plane of polarization of excitation and the absorption transition dipole moment. This increasing degree of photo-selection with $i$ can also be expressed as [28]:

$$R_{0i} = \frac{2i}{2i+3}\left[\frac{3}{2}\,cos^2\,\beta_i - 1/2\right] \qquad (15)$$

where $\beta_i$ is the intramolecular angle between the absorption and emission transition moments. Equation 15 describes the maximum dynamic range of anisotropy measurement which, in the collinear ($\beta_i = 0$) case, is $R_{0i} = 0.4$ for $i = 1$, 0.57 for $i = 2$ and 0.67 for $i = 3$. This increase in initial anisotropy facilitated by multiphoton excitation is potentially very powerful when resolving complex rotational kinetics (i.e., more than one rotational correlation time), and when the fluorescence lifetime is significantly less than the rotational correlation time. The power of using 2-photon excitation to extend the dynamic range of depolarisation can be seen in Fig. 2.

## EXPERIMENTAL

A range of sodium silicate solutions (silicate liqueurs, commonly referred to as *water glass*) are commercially available for hydrogel synthesis with differing densities and mean mole or weight ratios, that is, ($Na_2O$:$SiO_2$). We have used a 79.5 Twaddle*, 3.3 weight ratio, sodium silicate solution ($Na_2O.3.3SiO_2.H_2O$) supplied by Crosfield Chemicals Ltd. (trade name, Crystal 79), now Ineos Silica's.

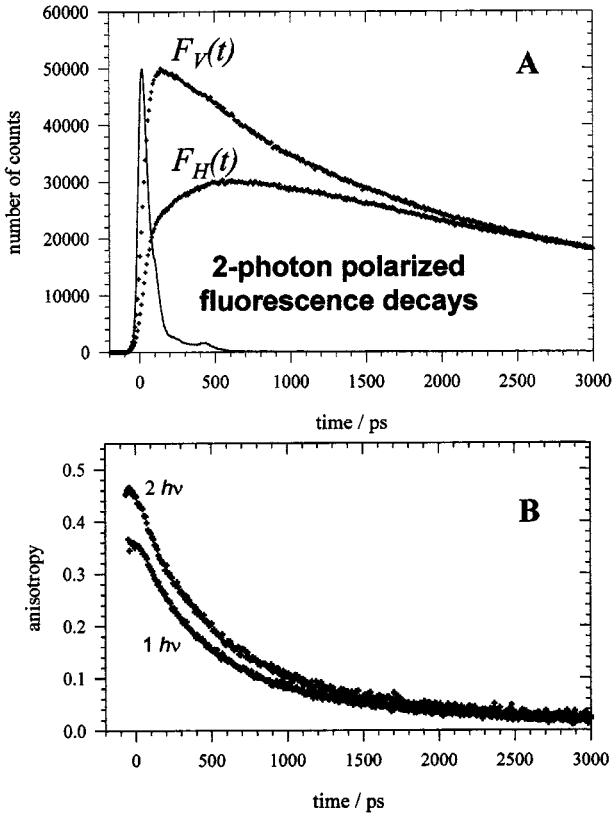


**Fig. 2.** (A) 2-photon polarized fluorescence decays and instrumental response function and (B) corresponding 1- and 2-photon anisotropy decays *R(t)* for the TMOS sol doped with rhodamine 6G at 41663 min. The channel width is 8.7 ps and instrumental response function < 100 ps fwhm. Data from Karolin *et al.* [23].

Solutions of different densities were obtained by diluting Crystal 79 with doubly distilled deionized water. The % $Na_2O$ in sodium silicate solution was determined by titration with HCL (Eq. 16), whilst the % $SiO_2$ was determined by titrating the NaOH liberated from the reaction of $Si(OH)_4$ with NaF, with HCl (Eq. 17).

$$Na_2O + 2\,HCl \rightarrow 2\,NaCl + H_2O \qquad (16)$$

$$Si(OH)_4 + 6\,NaF \rightarrow Na_2SiF_6 + 4\,NaOH \qquad (17)$$

The percentages of $Na_2O$ and $SiO_2$ in 79.5 Twaddle sodium silicate solution, obtained by titration, and its subsequent dilutions are shown in Fig. 3. For comparison percentages in other commercial sodium silicate liqueurs are also shown.

Fluorescence studies of the sodium silicate solutions revealed complex decay kinetics with multiple emitting species evident [Fig. (4)]. Subsequently, to alleviate water-glass autofluorescence all studies of hydrogels prepared from water glass were undertaken in the near-infrared.

*Twaddle—The *twaddle* ($^0$Tw) is a unit of density first used at the turn of the century to enable workers to easily deal with integers and is still readily used in industry today. SI conversion: Twaddle = (200(density/g $cm^{-3}$)−1).

### Instrumentation

Absorption measurements were performed on a Perkin Elmer UV/VIS spectrophotometer (Lambda 2). Steady-state fluorescence emission and/or anisotropy measurements were performed on a FluoroMax-2 (ISA Instruments New Jersey) equipped with dichroic sheet polarises (Halbo Optics).

For 1-photon near-IR studies (JA120, JA53, and Rhodamine 700 hydrogels), orthogonal polarized fluorescence decay kinetics were recorded using the time-correlated single-photon counting technique [29] in ≈2-minute measurement times at different times following initial mixing of the sol, as shown in Fig. 5. This incorporated a Hamamatsu PLP-02 diode laser for excitation and an EG&G CD2027 single-photon avalanche diode for detection. The 650-nm diode laser generated 70-m*W* vertically polarized optical pulses of duration ≈50 ps at 1-MHz repetition rate. The overall instrumental response function

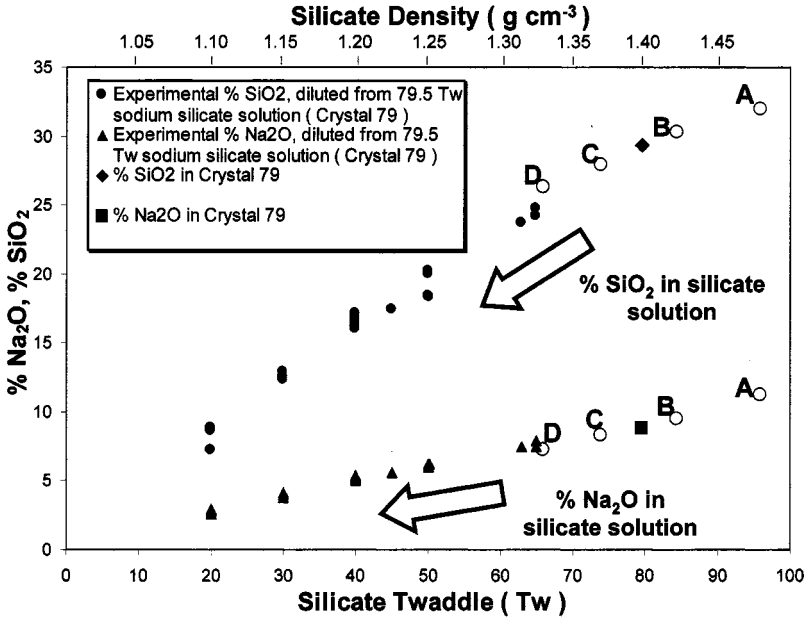


**Fig. 3.** Percentages of $SiO_2$ and $Na_2O$ in 79.5 Tw sodium silicate solution (Crystal 79) and dilutions of 79.5 Tw sodium silicate solution used to make sol-gels of different densities. Other commercial silicate liquors are shown. (A) Crystal 96 (96 Tw, weight ratio = 2.85); (B) Crystal 84 (84.5 Tw, weight ratio = 3.20); (C) Crystal 74 (74 Tw, weight ratio = 3.38); (D) Crystal 66 (66 Tw, weight ratio = 3.65).

was ≈350 ps fwhm. Fluorescence was selected using an IBH Model 5000M f/3 monochromator with a spectral range of 300–1200 nm, a Kodak 720 nm cut-off filter, and a dichroic polarizer (Halbro Optics).

Two- and white-light one-photon femtosecond excitation (for Rhodamine 6G TMOS sols) were achieved using a Coherent RegA 9000/Mira 900 regeneratively amplified Ti:Sapphire laser (repetition rate 250 KHz; excitation pulse duration ≈120 fs; center-wavelength 800 nm; energy per pulse ≤4 μJ). The fluorescence anisotropy decay curves were again collected using the well-known time-correlated single photon-timing technique [29]. The instrument and measurement of multiphoton excited fluorescence anisotropy decays have been described previously [30], recent additions being a faster photon timing detector (Hamamatsu cooled MCP-PMT model R3809U-50) and discriminator (EG&G Ortec model 9327) (Fig. 6). The overall instrumental response was ≈100 ps fwhm. Two-photon excited R6G fluorescence was wavelength selected by using an 800-nm cut-off filter, which excluded the laser fundamental. The laser power dependence of the fluorescence confirmed the 2-photon nature of the excitation for those respective experiments [30].

For the time-resolved 1-photon excited fluorescence experiments for the R6G TMOS sols, white light was generated in a Ti:sapphire glass plate. The excitation wavelength from the white light continuum was selected by a 500- ± 10-nm interference filter (Comar Instruments, UK) and fluorescence emission observed through a 550-nm long-pass filter. For all experiments the temperature was regulated at 20 ± 1 °C. The typical measurement time taken to record the anisotropy decay was ≈30 min, sufficient to accumulate a maximum count per channel of 10,000 to 20,000 in the difference function $F_V(t) - F_H(t)$ [cf. Eq. (9)]. Although 30 min at first may seem a long measurement time, it should be noted that in this case the TMOS sol gelation time was 56160 → 59040 min.

To compare our studies with typically non-gelling sols, a Ludox colloidal silica (Du Pont's AM30, 30% w/w $SiO_2$, 6-nm radius, pH 8.9) was labeled with CG437, a 6-methoxyquinoline-type dye that we have recently synthesized for this purpose [22]. For CG437, 1-photon excitation was provided at 370 nm by means of nanosecond pulses from an IBH NanoLED operating at 1 MHz and at 400 nm by the femtosecond frequency-doubled Ti:sapphire laser.

Non-linear least squares impulse reconvolution analysis of the anisotropy data [29] was performed using the IBH Ltd Fluorescence Lifetime System 5000 software library. The procedure for impulse reconvolution corrects for distortion resulting from the finite instrumental

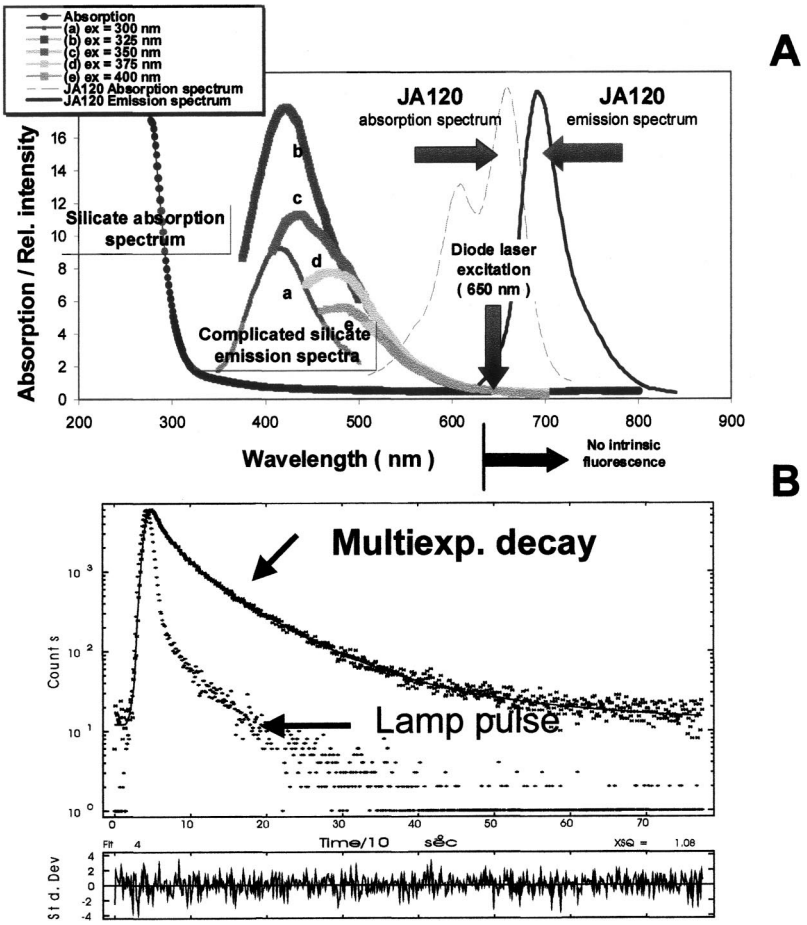


**Fig. 4.** (A) Absorption and steady-state emission spectrum of Crystal 79. Also shown is the absorption and emission spectrum of JA120 used to probe low-pH sodium silicate–based hydrogels. Near-IR 650-nm LD excitation can be seen to alleviate silicate background fluorescence. (B) Multiexponential fluorescence decay of Crystal 79 recorded in the TD using TCSPC. $\lambda_{ex}$ = 300 nm.

response. This first involves fitting to the fluorescence decay given by; $F_v(t) + 2F_H(t)$, [the denominator in Eq. (9)] and obtaining the corresponding fluorescence impulse response function, I(t). The product of I(t) multiplied by iterations of R(t) are then convoluted with the measured instrumental response function and fitted to the measured difference data [the numerator in Eq. 9], $F_v(t) - F_H(t)$, using non-linear least squares, with a minimization of chi-squared ($\chi^2$) goodness of fit criterion. A normalized $\chi^2$ value close to unity indicates the absence of systematic errors and an appropriate anisotropy decay model [R(t)] described by the best fit parameters, for example, $\tau_{r1}$, $\tau_{r2}$, $R_0$, f. For all the measurements the samples remained optically transparent such that depolarization resulting from multiple scattering from particles and pores can be neglected. Magic angle polarization, 54.7° [9] was selected for all fluorescence lifetime measurements.

## Silica Hydrogel Preparation (<pH 2)

Silica hydrogels were prepared using the continuous flow preparation system (sol-gel rig: made in-house), (Fig. 7). Two glass water-jacketed vessels (Aldrich Chemical Co.), containing $H_2SO_4$ and sodium silicate solution are maintained at 20 °C. Two (Watson-Marlow 505S/rl) peristaltic pumps deliver both acid and silicate solutions through Marprene tubing to a stainless steel mixing head (Fig. 8). By varying both concentrations and the pump speeds, sols differing in $\%SiO_2$, pH, and therefore gelation time (denoted $t_g$) can be produced. Table I shows

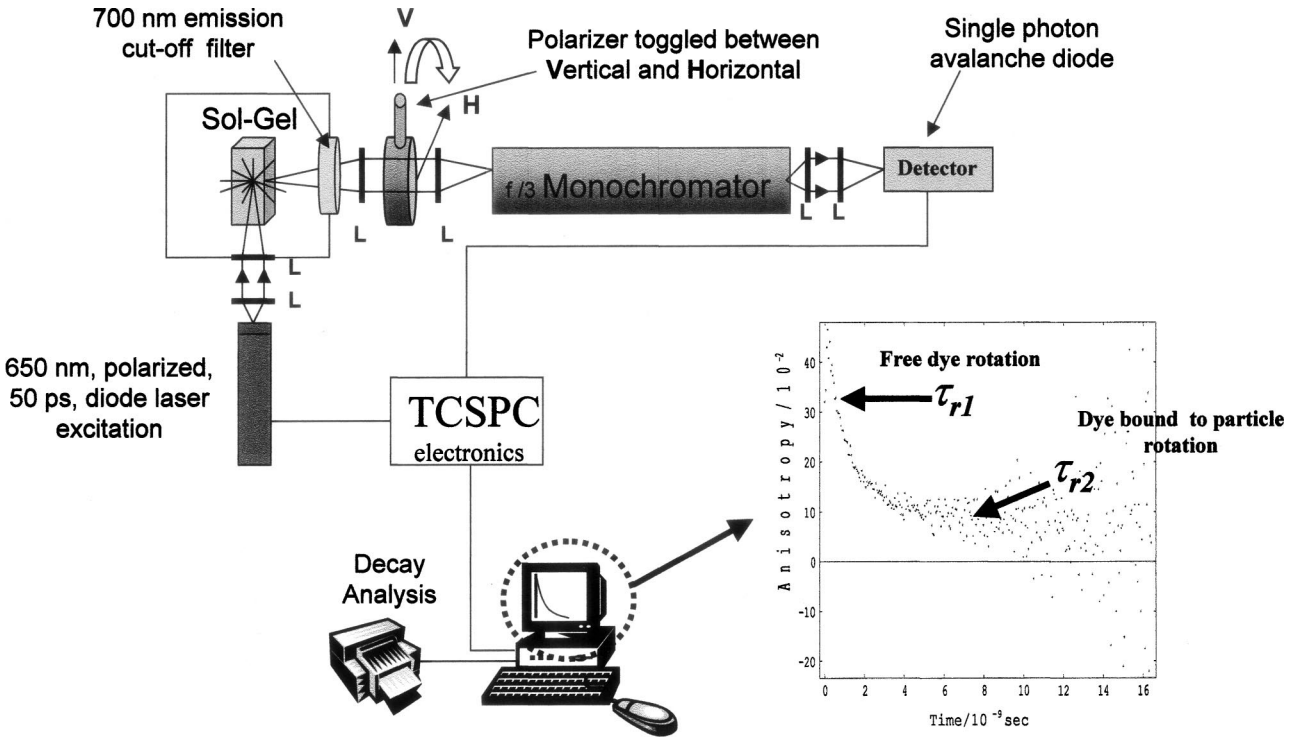


**Fig. 5.** Fluorescence anisotropy decay measurement of silica hydrogels using time-correlated single-photon counting. L-lenses. From Geddes and Birch [17].

some typical flow parameters and reactant concentrations used to produce various sols.

Three different mixing heads have been developed. Figure 8A shows the standard mixing head (bottom view) in which two stainless steel tubes deliver $H_2SO_4$ and sodium silicate solutions together to the propeller, operating at 1200 rpm. A change in bore size and a jet nozzle further aid mixing in the head. In this standard setup, the sol can be doped with fluorophore at the final collection point. The second mixing head allows the dilution of the sol by the introduction of water via a third inlet pipe (Fig. 8B), whilst figure 8C shows how the mixing sol can be continually doped by the small additional of an aqueous probe using either a syringe or suitably small peristaltic pump. When in use the mixing head

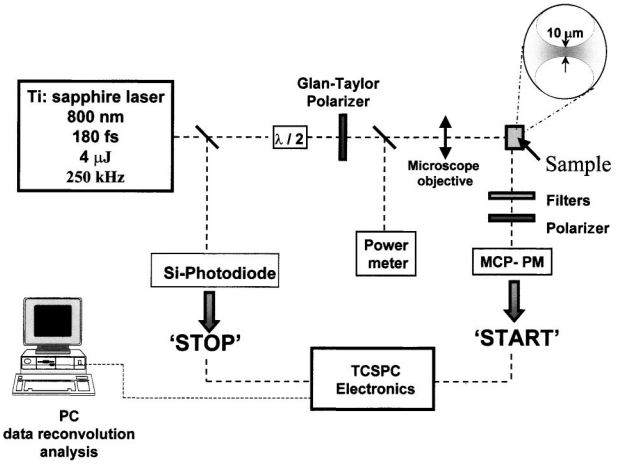


**Fig. 6.** Fluorometer for anisotropy decay measurement based on multiphoton excitation using femtosecond laser pulses and reverse start-stop time-correlated single-photon counting detection. From Karolin *et al.* [23].

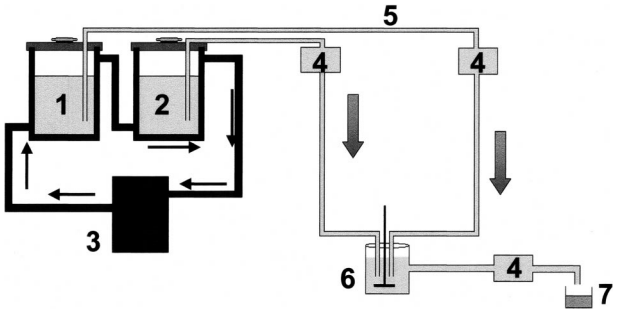


**Fig. 7.** Continuous flow system for the preparation of acidic hydrogels (sol-gel rig). (1) Sodium silicate solution (water glass); (2) sulphuric acid; (3) thermostat; (4) peristaltic pumps; (5) Marprene tubing; (6) mixing head vessel; (7) sol-gel. From Geddes and Birch [17].

**Table I.** Sol-Gel Flow Parameters and Reactant Concentrations Used

| Initial % silicate | Initial °Tw silicate | Initial % acid | Initial °Tw acid | Silicate flow rate $mL^{-1}$ | Acid flow rate $mL^{-1}$ | Excess acid normality in sol-gel, N, pH | Final % $SiO_2$ in sol-gel | $t_g$ (min) |
|---|---|---|---|---|---|---|---|---|
| 20.21 | 50 | 34 | 50.2 | 7.58 | 2.43 | 0.27N, pH 0.87 | 15.30 | 60–74 |
| 16.94 | 40 | 28 | 40 | 7.58 | 2.53 | 0.25N, pH 0.90 | 12.70 | 240–270 |
| 12.50 | 30 | 22 | 30 | 7.25 | 2.66 | 0.31N, pH 0.81 | 9.14 | 990–1050 |
| 8.62 | 20 | 15 | 20 | 6.76 | 2.92 | 0.30N, pH 0.82 | 6.02 | 2760–3240 |

SI conversion = Twaddle (°Tw) = 200(density/g/$cm^{-3}$ −1). The final sol compositions were calculated by using Eqs. (18)–(25). Data from Geddes and Birch [17].

is typically positioned off-centre, ≈1 cm from the bottom of the mixing head vessel. A centrally positioned mixing head results in a deeper solution vortex that can cause aeration and splashing of the hazardous material and even allows unmixed material to be collected at the 300-mL outlet level.

The choice of mixing head screens (Fig. 9) is an important consideration because the optical quality of sols can depend on the extent of aeration of the sol. In addition the ability to mix the reactants together efficiently, which is the mixing head's prime function, can be dependent on the screen mesh size, particularly at high silica concentrations. In contrast, some screens produce inhomogeneous sols (regions of differing pHs), causing premature or localized gelation. Typically, a standard emulsor screen or square-hole high-shear screen (Silverson) (Figs. 9B and C is used on the mixing head, keeping aeration to a minimum but also producing a homogeneous sol. In our case, the Silverson general purpose disintegrating head, shown in Fig. 9A, does not emulsify the sol well enough, in contrast to the fine emulsor screen (not shown), which extensively aerates the sol.

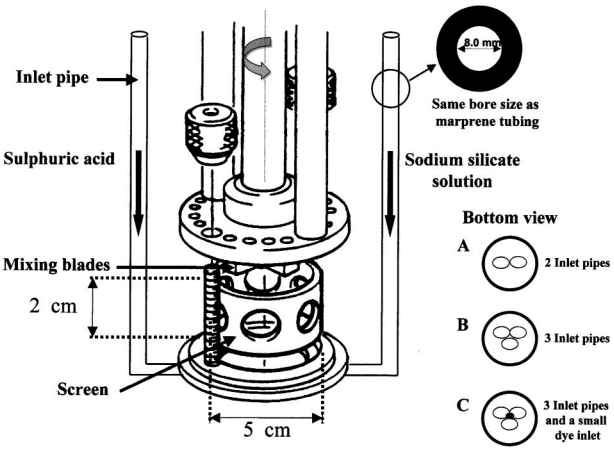


**Fig. 8.** Stainless steel mixing head. A slight change in bore size and angled nozzles direct the solutions for maximum mixing efficiency, which can be verified by the consistency of the sol gelation time ($t_g$). For further mixing efficiency the screen mesh size can be changed depending on the viscosity of the sol (Fig. 9). Also shown are bottom views of different acid-silicate-probe delivery mechanisms to the mixing blades. System A was typically used throughout this work.

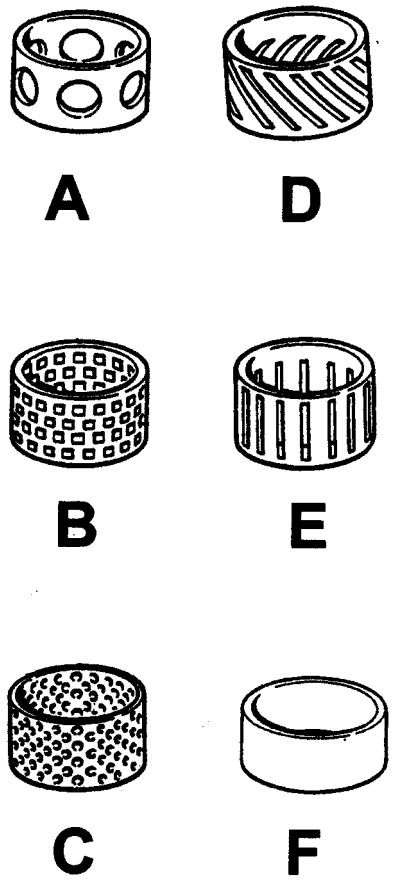


**Fig. 9.** Mixing head screens. (A) General purpose disintegrating head; (B) square-hole, high-shear screen; (C) Standard emulsor screen (produces homogeneous sols, the finer version of this head, *not shown*, aerates the sol; (D and E) slotted disintegrating heads. (F) axial flow head (Although this head expels material vertically upward, it is particularly good at reducing aeration in high density sol).

In a typical acidic hydrogel preparation, the acid pump delivers acid to the mixing blades for a given period of time, denoted the system-dead time, after which time the silicate pump is started. An acid dead time is necessary for two important reasons. Firstly, the alkaline silicate solution has to be quickly and efficiently made acidic so as not to gel in the mixing head. Second, the mixing head has a volume $<20$ cm$^3$ in which it has to initially acidify the sol. The mixing head vessel is also designed to have a mixing volume, typically 300 cm$^3$, before the sol is pumped away. This enables very efficient sol mixing, but typically requires many minutes for the acid concentration to drop to the required steady-state value. This inevitably consumes large volumes of reactants, producing large volumes of acidic waste. The next section describes how the composition of the sol is determined. One can further imagine some simple calculations showing how long the system should run, to correct for the initial acid dead time and 300 cm$^3$ mixing vessel volume.

*Calculating Sol Composition*

The initial reactant parameters such as % w/w, and the specific gravity (SG) of the acid and silicate, as well as the weight ratio of the glass, were predetermined by titration. The volumetric flow rates were determined by using either electronic digital flow meters (Cole Palmer) or by simply measuring the volume collected as a function of time. The following equations below, for use with the continuous-flow sol-gel preparation rig (Fig. 7), were used within a Microsoft Excel spreadsheet to determine final sol composition (see Table I)

*Mass Flow Rates*:

$$\text{Silicate (Kg/min)} = (\text{Flow rate (L/min)} * \text{SG}) \quad (18)$$

$$\text{Acid (Kg/min)} = (\text{Flow rate (L/min)} * \text{SG}) \quad (19)$$

*Excess Acid Present in Sol Emerging from the Mixing Head*:

$$\text{Mass flow rate of } Na_2O \text{ ex-mixing head (Kg/min)} = \left(\frac{\%\text{silicate}}{100 * \text{ ratio}}\right) * \text{Eq. 18} \quad (20)$$

$$\text{Empirical Excess acid (100 \%) (Kg/min)} = \left(\frac{\text{eq. 20}}{62}\right) * 98 \quad (21)$$

*Sol-Gel Rig Operating Conditions*:

$$\text{Actual mass flow rate of acid used (Kg/min)} = \text{Eq. 19} * \left(\frac{\%\text{acid}}{100}\right) \quad (22)$$

$$\text{Excess acid (Kg/min)} = (\text{actual-empirical}) = \text{Eq. 22} - \text{Eq. 21} \quad (23)$$

*Final Sol Composition*:

$$\text{Excess acid normality in sol (N)} = \frac{\text{eq. 23} * 1000}{\text{total flow rate(L/min)} * 49} \quad (24)$$

$$\%\ SiO_2\ (\text{w/w}) = \frac{\%\text{silicate} * \text{Eq. 18 (Kg/min)}}{\text{Eq. 18} + \text{Eq. 19(Kg/min)}} \quad (25)$$

## Gated Hydrogel Sampling (Method to Observe Initial Sol Formation Kinetics)

Observing the real-time growth of the silica nanoparticles $<1$ min into the polymerization was initially difficult to achieve as typical measurement times, needed to acquire both the vertical and horizontally polarized fluorescence decay curves, were in excess of 2 min. However, the authors have subsequently addressed this problem and have developed a gated continuous flow sol-gel preparation and optical flow cell system {Fig. (10)[24]}.

The different delay stages (delay times) for doped sol flow after initial mixing allow, in essence, gated sampling (in an analogous manner to an optical gate), which allows polarized fluorescence decays to be collected irrespective of the acquisition time, but more importantly, without the continued growth and/or aggregation of silica nanoparticles. Again orthogonal polarized fluorescence decay kinetics were recorded using the time-correlated single-photon counting technique [29] [Fig. (10)]. For all the measurements the sol remained optically transparent such that multiple scattering from the particles could be neglected. For studying a 12.01 % $SiO_2$ (w/w), 0.44 *N*, pH 0.66 sol, then 30% $H_2SO_4$ was prepared by diluting 2750 cm$^3$ 50% $H_2SO_4$ (Ineos Silicas) to 5307.87 cm$^3$ using doubly distilled deionized water. The addition of 85 mg rhodamine 700 produced a 30% $H_2SO_4$, $3 \times 10^{-5}$ mol L$^{-1}$ rhodamine 700 solution, which after mixing ($\approx$1:3 ratio of pump speeds) produced a $10^{-5}$ mol L$^{-1}$ rhodamine 700 sol. Acid concentrations were readily con-

firmed by titration with 1 *N* NaOH. Sodium silicate solution, 16.26 % $SiO_2$ (w/w), was prepared by diluting 6000 $cm^3$ Crystal 79 (29.25% $SiO_2$ w/w, Ineos Silicas) to 12038.81 $cm^3$, again using doubly distilled deionized water and then sealed. After 24 hr (to allow the depolymerization of initial silica Q species[#] to reach equilibrium) the silicate and acid solutions were confirmed again by titration and were then peristaltically pumped together using Marprene tubing (Watson Marlow), at a rate of 7.35 and 2.55 $ml/s^{-1}$ respectively, into the stainless steel mixing head and beaker (Fig. 10). It is important to note that for gated sampling the solutions are drawn from the bottom of the glass reaction vessel to minimize any dead volume and therefore dead time. The solutions were efficiently mixed, by the stainless-steel mixing blades rotating at 1200 rpm (Silverson), to produce a 12.01% $SiO_2$ (w/w), 0.44 *N*, pH 0.66 sol. Depending on the preparation parameters, such as reactant concentrations, temperature, pump speeds etc., sols differing in percentage weight of silica, excess acid normality, and pH can readily be produced by this gated procedure [24].

The sol output pump was flow matched to the sum of the rhodamine 700–doped sulphuric acid and sodium silicate solution pumps (i.e., 9.9 $ml/s^{-1}$), to maintain a system steady state, at which time a sol delay line was chosen, which combined with the tubing length and bore size (0.8 m*M* diameter), gave the time for the anisotropy measurement, (i.e., the gating time delay). The elevated temperature of the sol, resulting from the exothermic nature of the acid-base heat of neutralization, was measured on the bulk sol directly after flowing through the flow cell and was found to be slightly dependent on the gating tubing length. This temperature, ≈35 °C, can then be used in calculating the spherical silica particle sizes from the Stokes-Einstein equation:

$$\tau_r = \frac{\eta V}{kT} \tag{26}$$

where *k* is the Baltzmann constant.

It was found that increasing extents of scattering of the excitation light (evident as sharp spikes in the polarized decay curves, not short correlation times) occurred

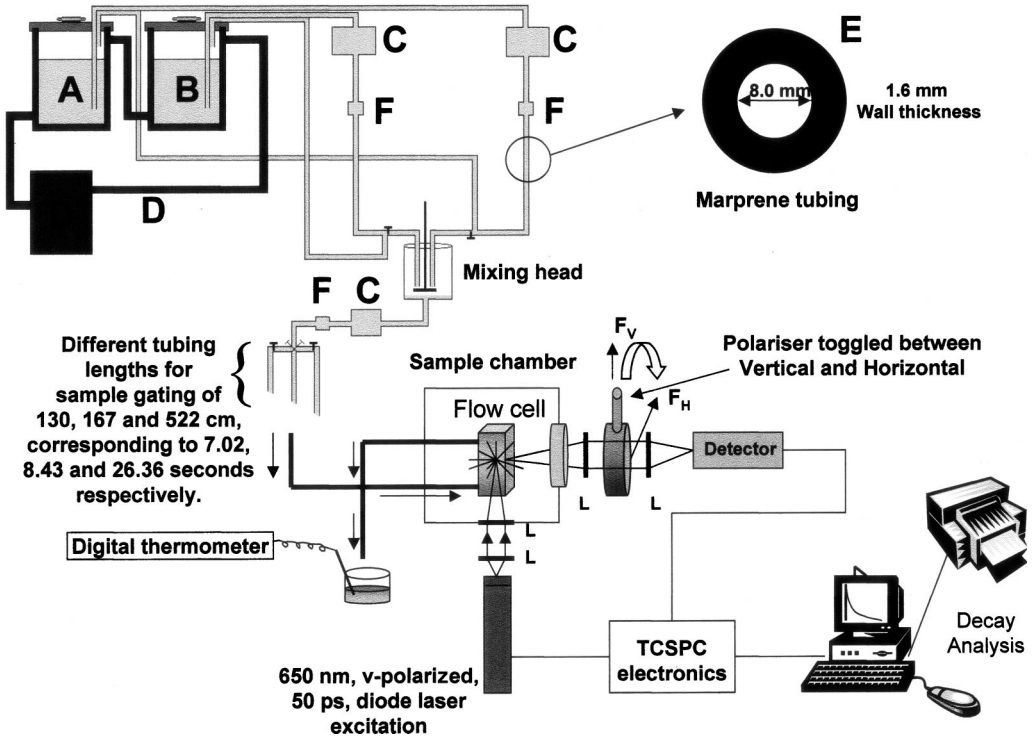


**Fig. 10.** Continuous flow sol-gel preparation system, flow cell, and time-correlated single, photon timing instrumentation. (A) 5307 $cm^3$ rhodamine 700–doped sulphuric acid; (B) 12,038 $cm^3$ sodium silicate solution; (C) Watson Marlow 505S/RL peristaltic pumps; (D) recirculating cooling bath at 20°C. (E) Marprene tubing. Ordinary tubing is not designed or suited for peristaltic pumping. The characteristics of the pump, including chemical suitability, suction lift, pressure, life, flow rate, and efficiency are largely determined by the tubing. 8.0-mm bore, 1.6-mm wall thickness tubing was used, which was a compromise between maximum tube life (using a large-bore tube at low speed) and maximum accuracy (using a small-bore tube at maximum speed). (F) Digital flow meters. Modified from Geddes *et al.* [24].

for very short gating times because of the extent of sol aeration. To alleviate this, different screen mesh sizes were used (Fig. 9), depending on the density of the sols being measured. As one would expect, the mesh size also affected the efficiency of initial sol mixing which was manifested in producing sols with slightly different gelation times, although this was only noticeable at high % w/w $SiO_2$ concentrations. In addition the bottom of the glass reaction vessel was tapered to prevent the sol-output pump drawing air (Fig. 11), with the additional use of Teflon plugs to minimize the finite volume of the taper.

In this gated study [24], rhodamine 700 was the probe chosen to track particle growth because it was found to be chemically stable in 30% (w/w) $H_2SO_4$, has a relatively small (radius $<$ 0.6 nm [31]), was rapidly taken-up by the growing silica nanoparticles in the acidic sol (similar behavior to that observed under other acidic and alkaline conditions [32]), as well as having a suitably short fluorescent lifetime, $\tau$, in the sol to resolve silica nanoparticle formation and growth, that is $\tau \equiv \tau_r$. For rhodamine 700 in this sol, $\tau = 1.83$ ns and $\chi^2 = 1.24$, at a gating time of 1 min.

For the gated sampling results shown in the discussion, vertically and horizontally polarized decays were measured using tubing lengths, measured from the bottom of the reaction beaker to the flow cell, of 139, 167, and 522 cm, corresponding to 7.02, 8.43, and 26.36 seconds, respectively.

[#]For $Q_Y^X$ species notation, the superscript *x* denotes the number of bridging oxygen's (−OSi) surrounding the central silicon atom and the sum of the subscripts, *y*, is the number of silicons comprising the silicate species, for example, for trimers, y = 3. In sodium silicate solution many Q species are present, but in our case $Q^3$ species are likely to prevail.

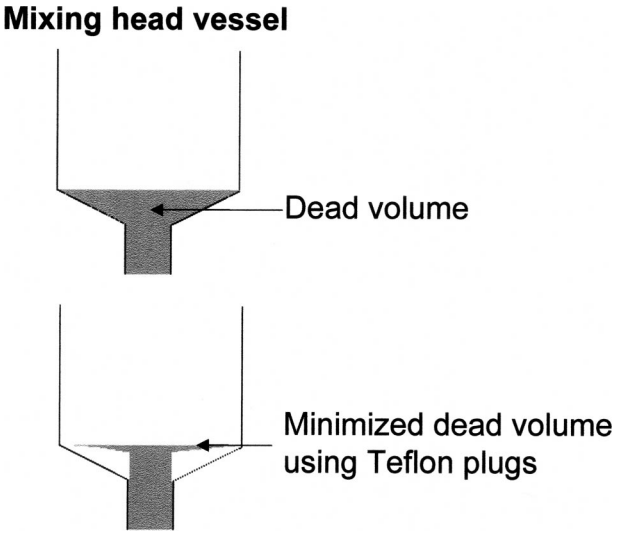


**Fig. 11.** The use of Teflon plugs to minimize the dead volume of the mixing vessel's taper.

### Preparation of Alkaline Hydrogels

Low % $SiO_2$ (w/w) alkaline hydrogels were prepared by firstly diluting Crystal 79 to the desired concentration and then slowly acidifying. Typically, dilute sulphuric acid was allowed to gravity feed into a baffled mixing beaker containing the sodium silicate solution, which was continually stirred. Because of the low density of the sols prepared by this method, elaborate and efficient mixing procedures, such as those employed for low pH hydrogel synthesis were not necessary. The $t_g$ for a 2% $SiO_2$ (w/w), pH 10 sol-gel at room temperature was $>$ 250 hr [32].

### Preparation of Silicon Alkoxide Sol-Gels

TMOS based sol-gels were made by mixing tetramethylorthosilicate, ethanol, water (doubly deionized), and HCl together to produce pH 2.3, 21.91% (w/w) $SiO_2$ sol-gels (based on complete polymerization of the reactants). The R value was 2, which under stoichiometric conditions would lead to complete hydrolysis and condensation [c.f. Eq. (8)]. Solutions were initially cooled to $<$4°C before hydrolysis to minimize any potential solvent boiling because of the exothermic nature of the reaction. A concentrated ethanol stock solution of R6G was used in the preparation to adjust the optical density of the sol to less than 0.1 at $\lambda_{abs}$max = 530 nm. Sol in the amount of 3.5 $cm^3$ was then cast into a quartz cuvette and sealed throughout to reduce drying and maintain a constant composition, as compared to the sol-gels made by Narang *et al.* [13], which were opened after 48 hr as part of an investigation into the drying process. The gelation time, $t_g$, was typically 56160–59040 min at ≈20°C, measured by observing the time for 15 mL sol to start peeling away from the sides of a sealed 50-mL glass sample bottle (Fisher Scientific UK) to the time when the sol had set firm.

### LUDOX Colloidal Silica

LUDOX AM30 colloidal silica was purchased from the Aldrich Chemical Company, Ltd. The silica particles in LUDOX are discrete, uniform spheres of silica that have no internal surface area or detectable crystallinity. The 6-nm radius particles are dispersed in a pH 8.9 alkaline medium (NaOH), which reacts with the silica surface to produce a negative surface charge, balanced with

sodium ions. In addition, some of the surface silicon atoms have been replaced with aluminium atoms, which creates a fixed negative charge, independent of pH, affording particle stability over the alkaline range [33] (Fig. 12). Because the particles repel one another, then they don't aggregate and hence the solution is typically non-gelling, which is ideal for testing the validity of our fluorescence nanoparticle metrology approach.

### Choice of Fluorescent Probes for Studying Sol-Gels

The choice of dye for labeling the silica particles is crucial and is influenced by several criteria. Ideally a dye should have a fluorescence lifetime comparable to the rotational correlation time of the particle, that is $\tau \equiv \tau_R$ [17,23] and constant when the dye is free in the sol and when bound to the particle. The dye should be stable at the pH used, have a good quantum yield (say $>0.2$), a high multiphoton absorption cross section when using multiphoton excitation and collinear absorption and emission transition dipoles, that is, $\beta_i = 0$ in order to maximize $R_0$ (cf. Eq. 15). Minimizing the dye size in comparison to the particle is also important. The dye should be water soluble for ease of depositing on the particle. Although functionality of the dye can be achieved to ensure covalent attachment to the silica [34], our experience is that other mechanisms (e.g., coulombic attraction) are often adequate. The isoelectric point and the point of zero charge of silica are in the pH range ≈1–3 [1,2], and therefore both anionic and cationic dyes have their uses. Inevitably a compromize in the choice of dye is usually necessary. The merits of the different probes used in this work are briefly described: rhodamine 6G is stable over a wide pH range, highly fluorescent, and readily taken up by silica and has a fluorescence lifetime ≈4 ns, which is compatible with nanometre particle rotational times in the sols studied and $R_{02}\sim0.57$. CG437 is cationic (charge balanced with a bromide counter-ion) and has solvent-dependent bi-exponential longer fluorescent lifetimes of ≈8.5–14 ns and ≈25–34 ns (Ludox AM30), making it more suitable than rhodamine 6G for studying particles of a 10-nm scale, but has $\beta_i \neq 0$, making $R_{01}$, $R_{02} < 0.4$. Figure 13A shows the 1-photon absorption and fluorescence spectra of an aqueous solution of CG437 and its molecular structure. Figure 13B shows the laser power dependence of the fluorescence intensity for CG437 labeled LUDOX AM30. The slope obtained supports the presence of 2-photon excitation [c.f. Eq. (13)]. It has also been shown previously that rhodamine 6G undergoes 2-photon excitation when excited at 800 nm [30]. It is interesting to note that the obvious step of frequency doubling the Ti:sapphire laser to obtain 1-photon excitation of rhodamine 6G at 400 nm results in an unworkably low $R_{01}$ value [30]. JA120 and JA53 (Fig. 14), were synthesised and supplied by Dr. Jutta Arden-Jacob, University of Seigen, Germany. Both JA120 and JA53 have similar absorption and fluorescence emission spectra (Peaking at ≈645 and 672 nm and 650 and 690 nm, $H_2O$/pH 7, respectively) and similar fluorescence lifetimes (≈1.83 ns and 1.76 ns, $H_2O$/pH 7, respectively). As briefly mentioned, near-infrared dyes are essential for studying sols made from sodium silicate solution and as such, both JA120 and JA53 were an ideal choice. Rhodamine 6G was used to study TMOS based sols, to compare with the findings of Narang *et al.*, [13], while CG437 was used to study the static LUDOX samples. Given the expense and availability of JA120 and JA53, rhodamine 700 was used in the gated sampling acidic hydrogel work, because 85 mg was required per ≈5.3 L acid solution, and also for probing high-pH hydrogels on chemical stability grounds.

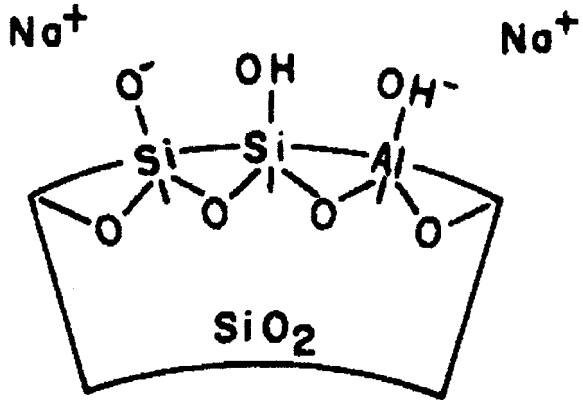


**Fig. 12.** Surface configuration of Ludox AM30 colloidal silica. From ref [33].

### Bulk Viscosity Measurements

Bulk viscosities, $\eta_b$, were typically determined for sols just up to $t_g$ and also for solvents in probe volume determinations, using two Ostwald Viscometers (Fisher Scientific) in the range 0–6 and 6–30 cP. The viscometers were initially calibrated with a standard of known viscosity and density at various temperatures, for example, water. For the viscosity measurements of sols the temperature was maintained at 20°C. The density of a 21.91% $SiO_2$ (w/w), pH 2.3, R = 2.00 TMOS sol at 1160 min, 20°C, was 0.923 g $cm^{-3}$ (mean of five measurements).

### Gelation Times, $t_g$

The $t_g$ values for the different sols were determined by noting the range of times when 1 L of sol (using the

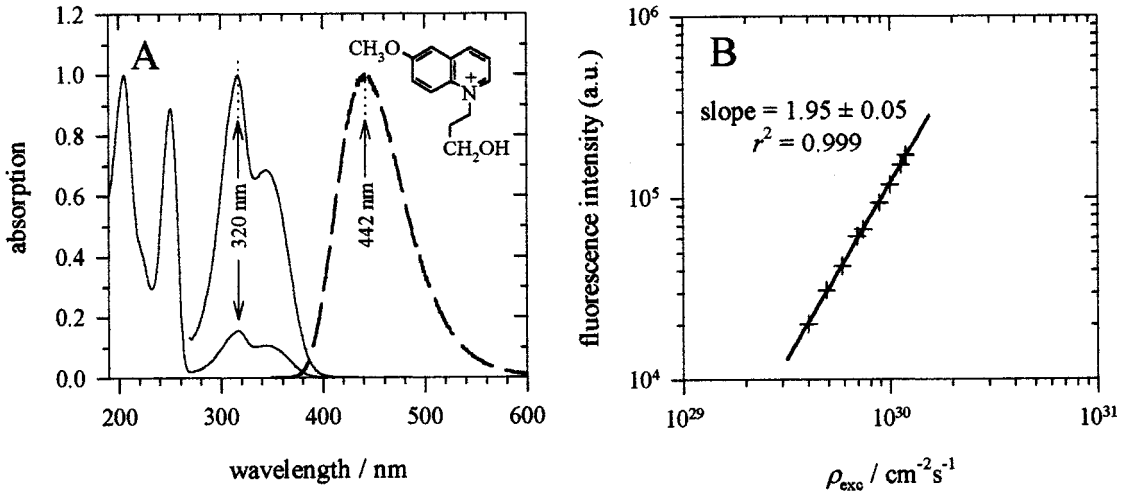


**Fig. 13.** (A) Absorption (—) and emission (–) spectra of a $10^{-5}$ M solution of CG437 in $H_2O$. The absorption spectra in the region 280–400 nm is expanded for clarity. Insert: Molecular structure of CG437. (B) Log-log plot of fluorescence intensity dependence of CG437-labeled silica particle (AM30) on the incident photon flux density at 800 nm. The regression coefficient is denoted τ. Data from Karolin *et al.* [23].

same Nalgene beaker) had thickened sufficiently to start peeling away from the sides of the beaker to the point when it could no longer flow and had set firm. For low-density sol-gels, $t_g$ is broader and greater than for higher-density (i.e. greater % w/w $SiO_2$) sol-gels containing the same excess acid normality.

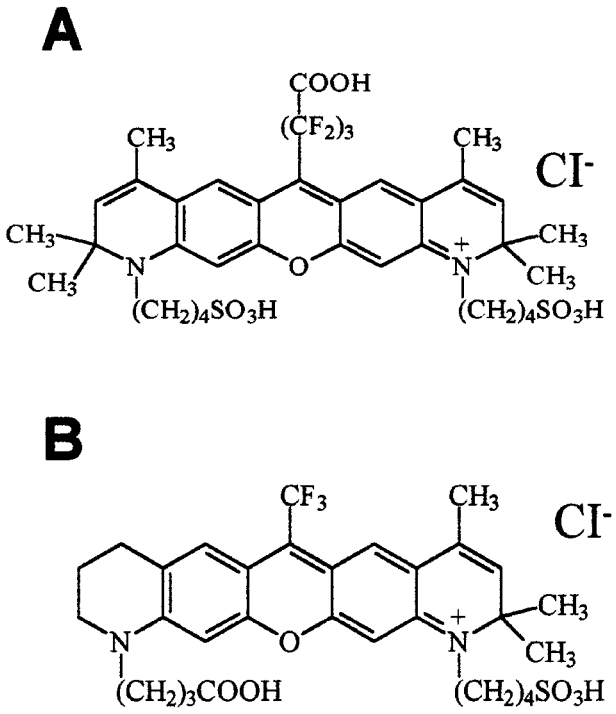


**Fig. 14.** Structural formulae for (A) JA120 and (B) JA53. $Cl^-$-counter ion.

## RESULTS AND DISCUSSION

Discussions of the nature of the second rotational correlation time, $\tau_{r2}$, whether a viscosity [13] or probe bound to growing silica nanoclusters (see Fig. 1), has been reported for both hydrogels [17,18] and TMOS [25]. The overwhelming evidence for the growing nanoparticle interpretation now allows us to discuss our results and interpretations in terms of sol kinetics and evolution for each of the sol-gel systems studied.

### Acidic Hydrogels

Figure 15 shows 1-photon anisotropy decays recorded for a JA120-doped 15.3% $SiO_2$, 0.27 *N* sol-gel (see Sol in Table I). We can clearly see a longer second rotational correlation time, with an increasing amplitude, as a function of the reaction polymerization time (pt) [c.f. Eq. (10)].

By using $\tau_{r1}$ to calculate the sol microviscosity [Eq. (26)] for the sols shown in Table I and using $\tau_{r2}$ we are able to calculate the growing silica particle size as a function of pt (Fig. 16). The initial aggregate growth shown in Fig. 16 can be well described to a first-order approximation (linear regression coefficient $R^2 \sim 0.96$) by a function of the form:

$$r = r_0 + (r_{max} - r_0)(1 - e^{-kt}) \qquad (27)$$

where the initial particle radius $r_0$ ranges from 1.4 nm to 1.7 nm (uncorrelated with $[SiO_2]$). For Fig. 16 (constant pH of ≈0.8–0.9 and varying silicate concentration) the

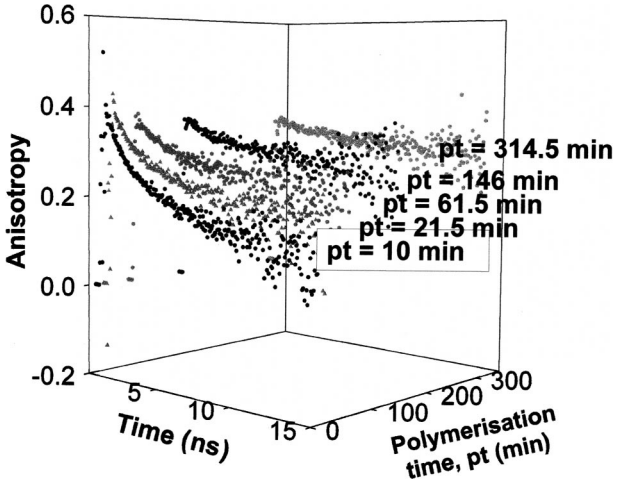


**Fig. 15.** Fluorescence anisotropy decay curves as function of polymerization time pt, for a 15.3% $SiO_2$ and 0.27 *N* sol-gel. Data from Birch and Geddes [18].

rate parameter *k* is $\approx 3.3 \times 10^{-5}$ $s^1$, $6.0 \times 10^{-5}$ $s^{-1}$, $8.6 \times 10^{-5}$ $s^{-1}$ and $1.7 \times 10^{-4}$ $s^{-1}$ for a 6.02% $SiO_2$ (weight for weight), 9.14% $SiO_2$, 12.7% $SiO_2$, and 15.3% $SiO_2$, respectively. Because the rise-times are faster, we have shown the time axis in Fig. 16 on a log scale.

A new aspect revealed by Fig. 16 is the peak after ≈2000 min. We attribute this to the intraparticle condensation rate ($\approx 6.0*10^{-6}$ $s^{-1}$, assuming an exponential reduction in particle radius) dominating the growth rate as the particle number density decreases. Shrinkage caused by condensation in a bulk gel is called syneresis and is well known [1,2], but until our recent work [17,18] had not been reported at the particle level. This is perhaps due to the limitations of scattering techniques for studying particles against a background of scattering from the gel. Ignoring particle syneresis may prove to be a major omission in current theoretical sol-gel evolution models.

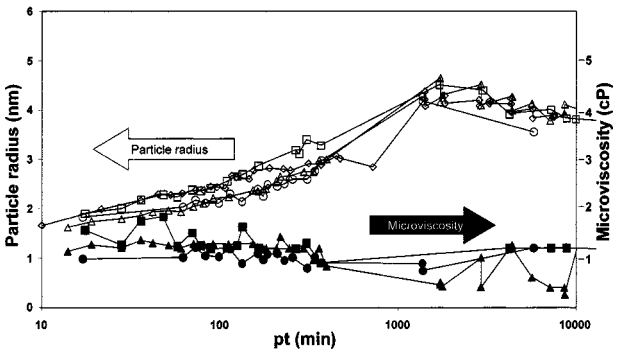


**Fig. 16.** Fluid microviscosity (solid symbols) and particle hydrodynamic mean radius (open symbols) as a function of polymerization time, pt, for 15.3% final $SiO_2$ concentration and 0.27 *N* excess acid normality (viscosity omitted for clarity, radius ◇), 12.7% $SiO_2$ and 0.25 *N* (■,□), 9.14% $SiO_2$ and 0.31 *N* (▲,△), 6.02% $SiO_2$, and 0.30 *N* (●, ○), sol-gels. The corresponding $t_g$ values are 60–74 min. 240–270 min, 990–1050 min and 2760–3240 min respectively. Data from Birch and Geddes [18].

It can be seen from Fig. 16 that the resolution we obtain, using JA120 as a probe, as the particles grow during polymerization is quite good, that is, at least as good as x-ray and neutron scattering, but at much lower cost, greater convenience, and simplified measurement. Also, unlike these other techniques, fluorescence anisotropy decay provides the microviscosity and particle measurements *in situ* at high silicate concentrations, even after the gel has formed. Also, the dye may be expected to intercalate within the ramified structures thought to describe the silica particles, contributing little to the overall hydrodynamic radius. To investigate probe effects further, we used another probe, JA53, under identical conditions. Subsequently, Fig. 17 shows a comparison of the growth functions for a 15.00% $SiO_2$ (w/w) sol-gel, pH 0.73, 0.37 *N* excess acid ($t_g$ = 68–74 min) using both JA120 and JA53, where both functions can be seen to be very similar. Interestingly, the smallest particle size that is measurable is determined by the dimensions of the dye, though at ≈4-nm particle radius, the dyes we have used contribute <1% to the total hydrodynamic volume. In other studies (unpublished) we investigated the growth curve as a function of when the sol was doped. We found that later dye addition tracked the particle growth identically, just as though the sol was initially doped at t = 0.

As previously mentioned, we associate $\tau_{r1}$ with the rotation of the probe in the fluid part of the sol and indeed in residual fluid in the gel. Hence, the microviscosity is significantly less than the bulk viscosity at all times. Figure 16 shows that the microviscosity is lowered slightly after gelation, and this would be consistent with loss of low molecular weight silicate species from the fluid. A microdomain of constant microviscosity of ≈2

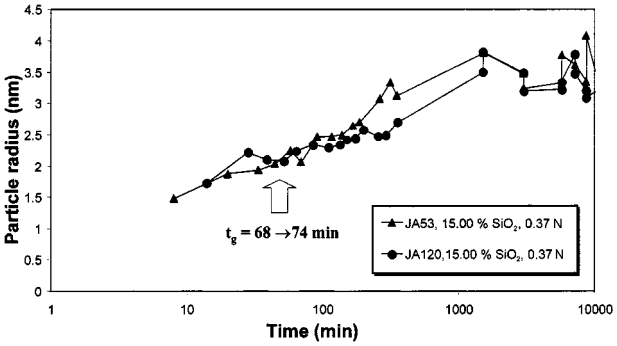


**Fig. 17.** Comparison of silica particle growth curves as probed by JA120 and JA53. Data from Birch and Geddes [20].

cP coexisting with a higher-viscosity microdomain, which increased in microviscosity from ≈10 to 1000 cP during polymerization, was proposed in previous work on alcogels [13] (see Fig. 1A). Our interpretation of the anisotropy decay in hydrogels differs from this mainly in that we account for the slower depolarization component in terms of the dye binding to silica particles (see Fig. 1B) [17,18].

The fraction, f, [Eq. (10)] has been interpreted as the fraction of fluorescence resulting from probe molecules bound to silica particles, and hence 1 − f the fraction resulting from free dye in the sol. However, the fractional intensities only give direct quantitative information when the anisotropies remain unassociated, that is, the quantum yield of the fluorophore remains similar when both free in the sol and bound to the growing silica nanoparticles. For all the sols studied by this approach, this was generally the case, the lifetime of JA120 changing only very slightly when bound. Figure 18 shows f for the sols in Table I increasing with silicate concentration and the duration of polymerization, which can be modeled according to:

$$f \approx f_0 + (f_{max} - f_0)(1 - e^{-ct}) \qquad (28)$$

with $c \approx 10^{-4}$ $s^{-1}$. The modeling necessity for $f_0 \neq 0$ probably just reflects the non-diffusion controlled take up of the dye at t = 0, although clearly in reality, $f_0 = 0$. Similar trends have also been reported by the authors for a variety of other sols produced from sodium silicate solution [15–22,24,26,32,35]. It is interesting to note that by stopping the polymerization at different times, by precipitating out the silica on addition of methanol, produced solutions containing different concentrations of dye. This is consistent with Eq. (28) and the take-up of dye as the polymerization proceeds, further supporting dye partition between the sol and growing silica nanoparticles.

The primary particle hydrodynamic radius in Fig. 16 is slightly greater than that reported for silica gel [4,36] using small-angle x-ray scattering, suggesting that water bound to the particles may contribute to the hydrodynamic radius under these conditions (i.e., pH, etc.), given that the probes are thought to be intercalated. The effect of hydrogen bonded water on silica hydrogel polymerization is an uncharted area that we have been able to study using $D_2O$ in an attempt to disrupt hydrogen bonding but not alter sol compositions or solubility, etc.

Figure 19 shows particle growth in the absence and presence of the addition of an equal volume of $D_2O$ or $H_2O$ to an equal volume of 15.11% $SiO_2$ (final w/w) sol-gel with an excess acid pH of 0.76. The corresponding $t_g$ values were ≈26 ± 1.5 and 21 ± 1 hr for the $D_2O$ and $H_2O$ additions, respectively. The $t_g$ of the undiluted sol was 48–55 min. The addition of $D_2O$ is seen to reduce the hydrodynamic radius, which could be caused by a reduction in hydrogen bonding on adding $D_2O$, corresponding to ≈2–3 water molecules, solubility differences during early ripening, or the microviscosity differences of the sol (1.26 cP for $H_2O$ addition as compared to 1.59 cP for $D_2O$ addition), influencing the relative diffusion rates of silica particles. Figure 20 shows that the fluorescence kinetics in terms of the rate of take up of the dye JA120 as reported by f is the same in the absence and presence of $D_2O$.

We sought to test our fluorescence anisotropy metrology approach further by adding salts to the initial sol and noting the effect on particle size. The addition of salts is well known to reduce $t_g$ because of the change in sol ionic strength, which reduces the surface charge

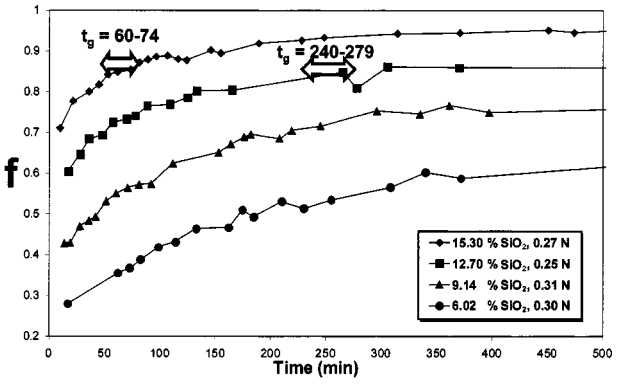


**Fig. 18.** The fraction f of total fluorescence due to dye binding to silica particles vs. time (pt) for the sol-gels in Table I. Data from Geddes and Birch [17].

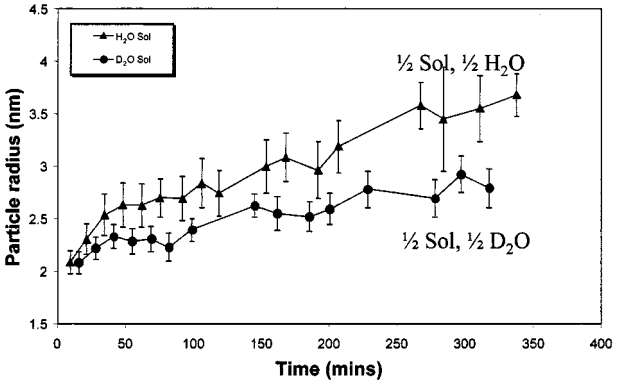


**Fig. 19.** Silica particle growth in the absence and presence of $D_2O$, using JA120, vs. time (pt). Errors in silica particle radii were calculated from three times the standard deviation of the bound dye rotational correlation time, $\tau_{r2}$, [c.f. Eq. (10)]. Data from Birch and Geddes [20].

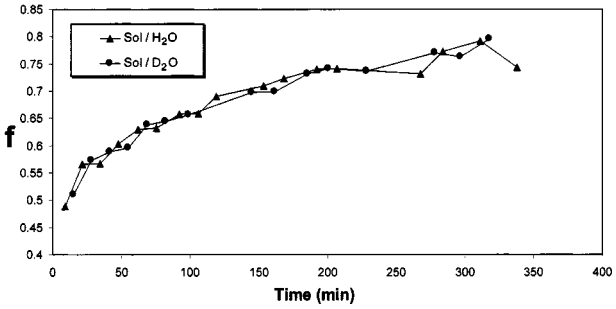


**Fig. 20.** Fluorescence fraction, f, due to JA120 bound to silica particles in the absence and presence of $D_2O$. Data from Birch and Geddes [20].

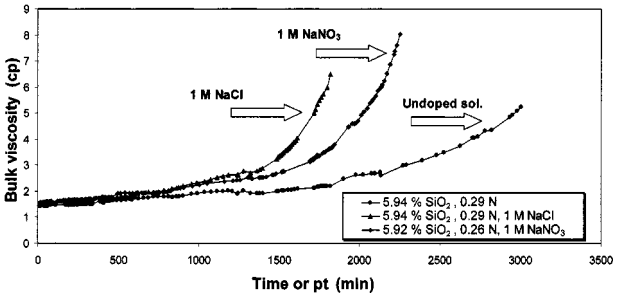


**Fig. 21.** The effect on the bulk viscosity and hence $t_g$ by adding inorganic salts. 1 M $NaNO_3$ and 1 M NaCL sols were prepared by adding 4.25 g and 2.92 g of the respective salts to 50 mL of sol containing $10^{-5}$ M JA120. Bulk viscosities were recorded using Ostwald Viscometers. Data from Birch and Geddes [20].

and mutual repulsion of silica particles and hence increases the interparticle condensation reaction rate [1,2]. Figure 21 shows the effect on the bulk viscosity (measured with an Ostwald Viscometer) by the addition of NaCl and $NaNO_3$ compared to the original sol. Table II shows the effect on the kinetic parameters of Eq. (27) by adding NaCl and $NaNO_3$. Little change in the initial primary particle radius of ≈1.7 nm was observed. There is little change in the growth rate, k, even though $t_g$ changes quite markedly on the addition of salt. The addition of NaF produced rapid gelation that was too quick to be studied by this method; however, gated sampling may aid studies in this regard.

The sequence of events leading up to the formation of silica gel at low pH, revealed by our new approaches and measurements [15–26,32,35] and in partnership with current sol-gel opinion [1,2], is summarized in Fig. 22. Initially, a few tetrahedra of monosilicic acid, $Si(OH)_4$, are joined together through siloxane (-Si−O−Si-) bonds formed in condensation reactions to give primary particles of mean radius ~1.5 nm. These primary particles diffuse through the sol, collide, and bond together by means of siloxane bonds formed through more condensation reactions. Secondary particles are thus formed through aggregation until a maximum mean radius of ~4.5 nm is formed. A simple volume calculation predicts the secondary particles to be composed of a maximum of ~13 primary particles. The aggregation rate eventually slows as the free particle number density decreases and there are few external hydroxyl groups available for collisions to result in further bonding between particles. The intraparticle condensation rate then dominates over the aggregation rate as internal hydroxyl groups continue to condense to form siloxane bonds, explaining the decrease observed from 4.5 nm to 4 nm (see Fig. 16). Eventually all but any sterically hindered internal hydroxyl groups are used up.

The usefulness of the silica particle growth curve shown in Fig. 16 from an industrial viewpoint lies in the fact that by stopping the polymerization process at a known precalibrated particle radius may lead to quality control of the surface area. From a theoretical viewpoint the growth curve provides new data for developing dynamical models, which in turn might lead to optimization of the sol-gel process in general.

**Table II.** Effect of Inorganic Salt Addition on the Parameters of Eq. 27

| Sol-gel/added salts | $r_0$ (nm) | k ($s^{-1}$) | $t_g$ (mins) |
|---|---|---|---|
| [a]5.94% $SiO_2$, 0.29 N(Pure sol) | 1.81 ± 0.05 | $2.36e^{-5}$ | 2803–3013 |
| 5.94% $SiO_2$, 0.29 N(0.1 M NaCl) | 1.77 ± 0.02 | $3.36e^{-5}$ | 2743–2833 |
| 5.94% $SiO_2$, 0.29 N(1 M NaCl) | 1.69 ± 0.15 | $3.94e^{-5}$ | 1823–1883 |
| [a]5.92% $SiO_2$, 0.26 N(Pure sol) | 1.70 ± 0.04 | $2.27e^{-5}$ | 2895–3045 |
| 5.92% $SiO_2$, 0.26 N(0.1 M $NaNo_3$) | 1.71 ± 0.03 | $2.25e^{-5}$ | 2820–2910 |
| 5.92% $SiO_2$, 0.26 N(1 M $NaNO_3$) | 1.70 ± 0.03 | $2.45e^{-5}$ | 2580–2640 |
| 5.92 % $SiO_2$, 0.26 N(0.1 M NaF) | — | — | ≈8 |

$r_0$ = initial silica particle radius; k = initial aggregate growth rate (the linear regression coefficient $R^2$ was better than 0.97 for all the above data); $t_g$ - gelation time (the time for the liquid, the sol, to set firm).

[a]Both the 5.94% $SiO_2$, 0.29 *N* and the 5.92% $SiO_2$, 0.26 *N* sol-gels can be considered equivalent for comparison purposes. Data from Birch and Geddes [20].

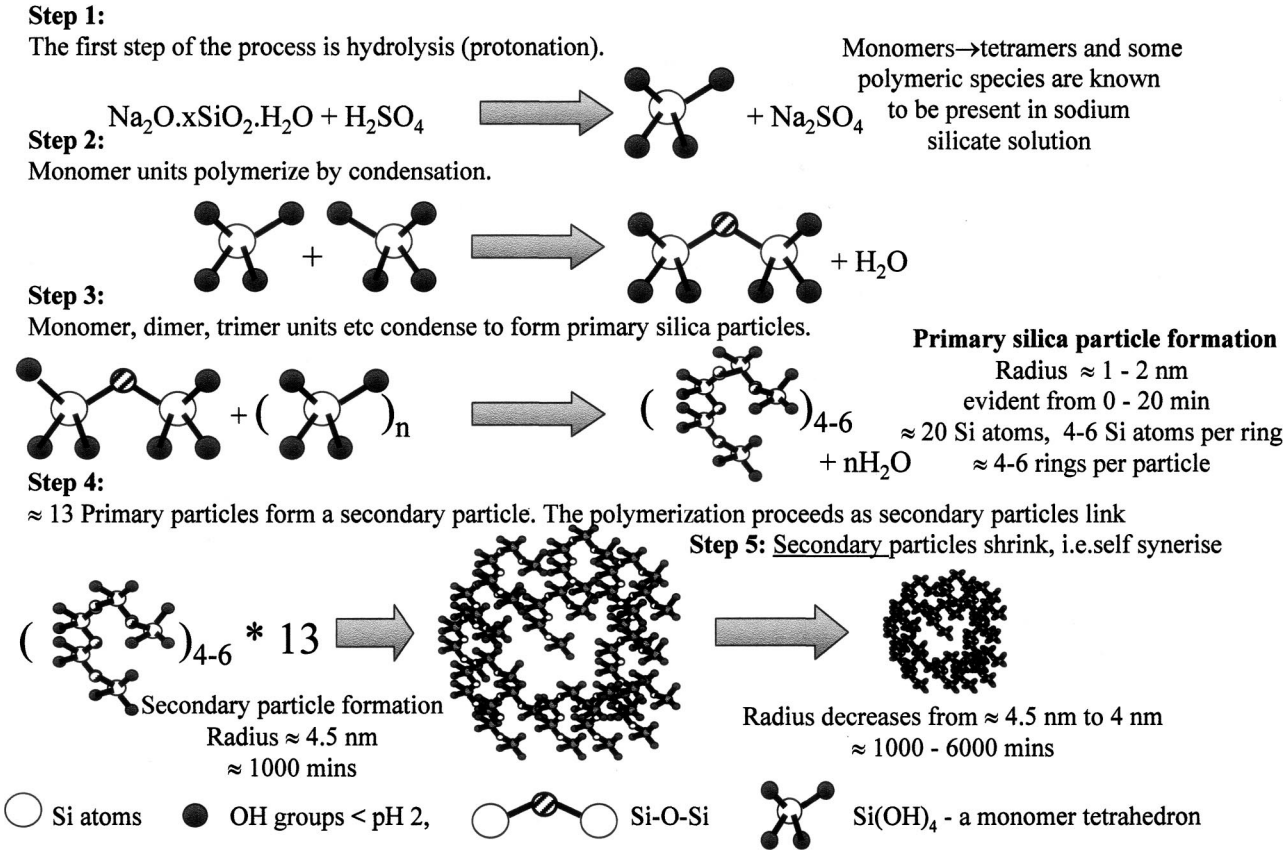


**Fig. 22.** The sequence of events leading up to silica hydrogel formation at low pH. Updated from Birch and Geddes [19].

## Gated Sampling of Acidic Hydrogels

Figure 23 shows the fluorescence anisotropy decay curves as a function of gating time (7.02, 8.43, and 26.36 seconds) for the 12.01% $SiO_2$, 0.44 *N* sol. Table III shows the corresponding rotational correlation times, bound dye fluorescence fraction, f, and calculated silica nanoparticle radius. We can clearly see differences in the decay curves, showing an increase in silica particle size as the polymerization proceeds. It is interesting to see from Table III that rhodamine 700 is initially unbound in the sol, evident by a very fast rotational correlation time ≈100 ps, very similar to that reported for aqueous (pH 7) rhodamine 700 [31]. At later gating delays the probe is partitioned between the aqueous phase and bound to growing silica nanoparticles, where the fluorescence fraction, f, can be seen to increase to ≈32% in <27 s. It is interesting that the results show a silica particle radius of ≈1.5 nm, previously found after several minutes polymerization [17,18], is in fact present within 10 s of a silica hydrogel being formed. Although just three gating times within 30 s of initial mixing have been reported to date by the authors, it is envisaged that many more measurements can be taken, with even better real-time resolution by modifying the flow rates, tubing bore size, and sol viscosity, where the

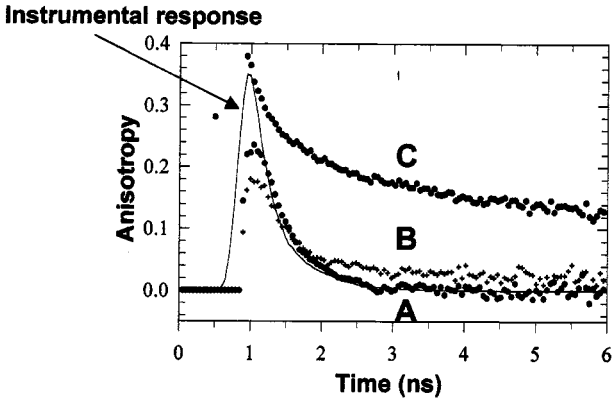


**Fig. 23.** Fluorescence anisotropy decay curves as a function of polymerization time, pt (or gating time) for a 12.01 % $SiO_2$, 0.44 *N* sol. A = 7.02, B = 8.43, and C = 26.36s, respectively. Data from Geddes *et al.* [24].

**Table III.** Kinetic Analysis of the Gating Delay Data

| Gating time (s) | $\tau_{r1}$ (ps) | $\tau_{r2}$ (ns) | f percent | $\chi^2$ | R (nm) |
|---|---|---|---|---|---|
| 7.02 | 97.3 ± 3.0 | — | — | 1.16 | — |
| 8.43 | 55.6 ± 3.5 | 3.0 ± 1.2 | 9.4 | 1.07 | 1.45 ± 0.14 |
| 26.36 | 108 ± 2.4 | 4.5 ± 0.2 | 32.4 | 1.20 | 1.66 ± 0.03 |

A microviscosity of 1 cP was used in the silica particle radius, R, calculation—indicates that a suitable fit to the data could *not* be obtained. f is the percentage dye bound to growing silica nanoparticles, calculated from the amplitude of the second rotational correlation time [c.f. Eq. (10). Data from Geddes *et al.* [24].

time resolution is independent of the sol mixing time, which was typically $<<<1$ second.

In summary, this approach of gated fluorescence nanoparticle metrology:

- Allows real-time silica nanoparticle measurements
- Allows the early formation dynamics of sol-gels to be realized, including the possibility of being able to distinguish discrete growth mechanisms such as Ostwald ripening or aggregation.
- Might allow real-time distributions of silica particles to be observed
- Could readily be applied to any sol-gel system, including tetraalkoxysilanes, for example, TEOS and the TMOS sol described in this paper, which are readily used in sol-gel research and photonic applications because of their better defined reactants compared to sodium-, potassium-, or lithium silicate–based hydrogels
- Can be used to measure other optical characteristics in real time, for example, absorption or emission spectra, steady-state anisotropy, etc., by mounting the flow cell in suitable instrumentation.

## Further Possibilities for Gated Sampling

Although this gated sampling approach allows the early formation kinetics of sol-gels to be observed, its principle drawback is the volume of sample required. For the 12.01% w/w $SiO_2$, pH 0.66 hydrogel less than 20000 $cm^3$ of reactants were used. This was due primarily to the mixing head and vessel, which were solely designed with efficient mixing in mind, but which required a finite dead volume to fill it. Whereas sulphuric acid and sodium silicate solutions are relatively cheap to mass purchase, if one wanted to apply this system to an orthosilicate sol, a considerable cost would be involved. However, it may be possible to mix the reactants efficiently using a variety of other methods, which and likely to substantially reduce reactant costs. For example, one could simply scale down the sol-gel rig, using smaller-bore tubing, smaller pumps, and a smaller mixing head. Such a system would be most attractive because some key metrology experiments could be undertaken, such as polymerizing dye-labeled TMOS under various conditions. Even donor–acceptor (for RET studies)-labeled TMOS (high-density) gated systems could be undertaken for studying very early TMOS self-assembly mechanisms.

## Alkaline Hydrogels

Figure 24 obtained at pH 10 shows a dramatic difference from Fig. 16 (at low pH) in respect of the former showing a clear bi-modal growth [32]. We have modeled Fig. 24 successfully using a function of the form [32]:

$$r = r_0 + (r_p - r_0)(1 - e^{-kpt}) + (r_s - r_p)(1 - e^{-kst}) \quad (29)$$

This function implies the growth of two different entities, one a precursor to the other, which reach different limiting radii, $r_p$ and $r_s$. One would typically ascribe $k_p$ as the rate of growth of a primary particle species resulting from a monomer addition and $k_s$ as the growth of secondary particles [1,2], again by monomer addition. However,

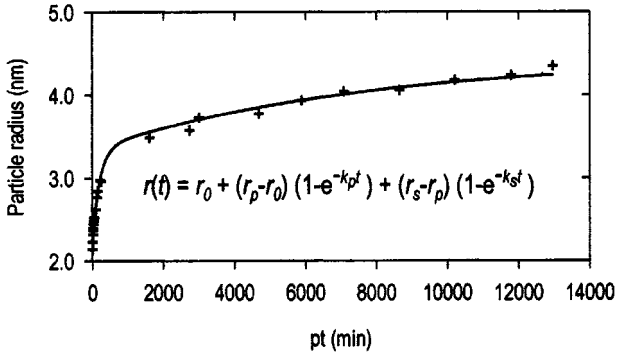


**Fig. 24.** Silica hydrogel particle growth at pH 10 for a 2% $SiO_2$ sol of $t_g > 250$ hr. Polymerization time (pt). Data from Birch *et al.* [32].

a single growth mechanism begs the question as to why two entities with distinct rates of formation are observed at all, and the role of cluster-cluster aggregation cannot be ruled out at early times because the growth rate ($k_p$) is close to that of $8.6 \times 10^{-5}$ $s^{-1}$ observed for secondary particles under acidic conditions at pH <1 [17].

Fitting to Eq. (29) gives $r_0 = 2.3$ nm, $r_p = 3.3$ nm, $r_s = 4.6$ nm, $k_p = 9.2 \times 10^{-5}$ $s^{-1}$ and $k_s = 1.9 \times 10^{-6}$ $s^{-1}$. According to this model, $r_0$ simply reflects the primary particle size in our first measurement and $k_s$ is just less than the syneresis rate measured under acidic conditions $\sim 6 \times 10^{-6}$ $s^{-1}$ (absent after 30 hr [17]) and may well reflect a net growth limited by intraparticle syneresis. Also, the author has reservations about the "open" and "branched" nature of sol particles typically associated with low % (w/w) $SiO_2$ sols, because their rotational dynamics are unlikely to be described well by Eq. (26).

Clearly, alkaline sols produced from sodium silicate solution are more complex to model, but can be resolved using fluorescence techniques. In this regard the gated sample approach [24], may allow different growth mechanisms in high pH sols, to be further observed and resolved.

### Tetraalkoxysilane (TMOS)-Based Sol-Gels

As discussed earlier the alkoxide "alcogel" route is the one that has been mostly used for research into sol-gel processes because it has better defined reactants and is typically simpler to prepare than a hydrogel. The polymerization of tetramethylorthosilicate (TMOS) has been studied previously using rhodamine 6G (R6G) and phase fluorometry and the anisotropy decay interpreted solely in terms of viscosity changes [13]. We have recently re-investigated this system using a slowly gelling 21.9% (w/w) $SiO_2$ sol at pH 2.3. At 20°C $t_g$ is $\sim 6 \times 10^4$ mins, and this gives plenty of time to maximise the anisotropy statistical precision during measurements in which negligible sol changes occur. The measurement precision was further enhanced by using a fluorometer (Fig. 6) capable of 2-photon excitation, increasing the initial anisotrophy [Eq. (15) and Fig. 2.

One of the advantages of the measurement technique we have developed is that Eq. (10) also gives the microviscosity of the sol, that is, from $\tau_{r1}$, and the particle mean radius. In contrast to our study of silica hydrogels using JA120, we found the fraction of fluorescence f due to dye bound to the particles for the TMOS sol, remained constant at ≈30% during the polymerization (Fig. 25). R6G is taken up very efficiently by silica, so on this evidence alone we cannot rule out the possibility that in fact all the dye is taken up and that the "free" dye rotation

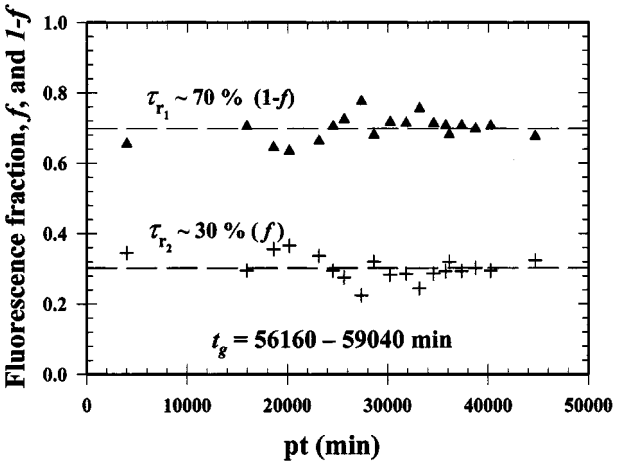


**Fig. 25.** Fraction of the total fluorescence $1 - f$ associated with the fast rotational correlation time $\tau_{r1}$, ▲, and $f$ associated with the slow rotational time $\tau_{r2}$, +, for the R6G-doped TMOS sol during polymerization. Data from Geddes *et al.* [25].

[((1 − f) in Eq. 10)] actually refers to dye tethered and wobbling on the particle. However, $\tau_{r1}$ is ~300 ps, that is, comparable with that for the free dye in the water/alcohol mixture we have found in the sol, and for the purpose of calculating the hydrodynamic mean radius the model given by Eq. (10) is independent of these alternative interpretations of f. Figure 26 shows how the calculated viscosity and particle mean radius change with polymerization time (pt). The viscosity values are similar in magnitude and show a slight downward trend with time, similar to that shown in Fig. 16 for a silica hydrogel at low pH [17,18], reflecting here the polymerization of the sol and the expulsion of methanol. The most notable feature of Fig. 26 is the smaller radius compared to anything we have so far detected in our metrology work,

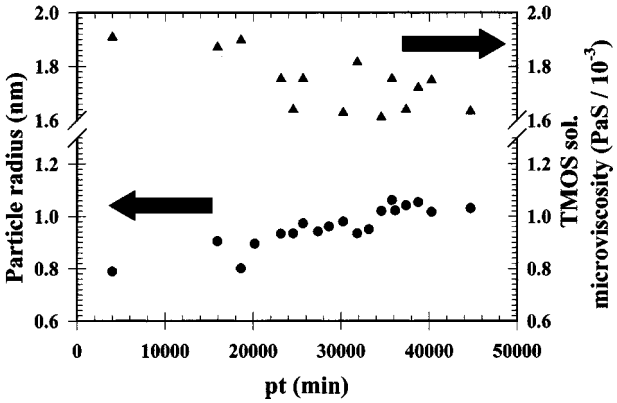


**Fig. 26.** Silica particle radius, ●, and sol microviscosity, ▲, as a function of polymerization time, pt, for the TMOS sol. The errors in particle radius were typically ± 0.1 nm. Data from Karolin *et al.* [23].

growing from ~0.8 to 1.1 nm and illustrating the high-resolution fluorescence anisotropy can offer. Clearly the small size reflects the different growth mechanism associated with monomer-monomer and monomer-particle addition in TMOS under these conditions rather than the secondary particle aggregation typically observed in hydrogels. We fitted the growth of silica hydrogels at pH <1 using $r \sim 1 - e^{-kt}$, [Eq. (27)], and attributed this to particle-particle aggregation (Fig. 16). For TMOS under these conditions, Fig. 26 can clearly be approximated by the limit of slow exponential growth at short times, that is, $r \sim kt$.

It is interesting at this time to comment on the notion of two microviscosity domains, fig. 1A, first proposed by Narang and co-workers [13] to explain the bi-exponential decay of fluorescence anisotropy of R6G doped TMOS sols. By interpreting our anisotropy data shown in fig. 26 also in terms of two discrete microviscosity domains, fig. 27, we can see that the second microviscosity, $\eta_2$, is much larger than the bulk viscosity, $\eta_b$, which if correct, would be expected to lead to a phase separation, but which was not observed.

### Particle Metrology on Static LUDOX Colloidal Silica's

To check the range of particle sizes that could be measured and compared with well-characterized colloids, we studied a Du Pont Ludox colloid labeled with CG437, namely LUDOX AM30. Because of the negative surface charge of the AM30 colloids, they repel one another, resulting in stable colloids, which is ideal to test the validity of our nanometrology approach.

Table IV compares the measured radii for 1- and 2-photon excitation (~7 nm) and the manufacturer's value (~6 nm) as reported on the LUDOX data sheet [33]. The ~1-nm difference may well reflect the influence of bound water on the hydrodynamic radius, which we measure, and indeed the contribution of the probe dimensions, given that the probe can not intercalate as is thought in the case of hydrogels. Alternatively, the quoted data sheet value of 6 nm may reflect the electron microscopy value obtained on the dried colloids.

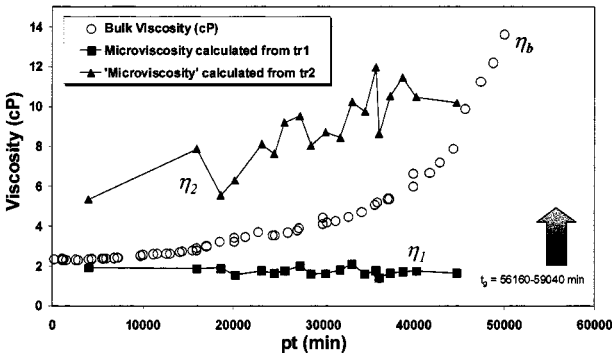


**Fig. 27.** Bulk viscosity, $\eta_b$ and microviscosities $\eta_1$ and $\eta_2$ determined from rotational correlation times $\tau_{r1}$ and $\tau_{r2}$, respectively [c.f. Eq. (10)], assuming they both relate to R6G rotating in two different fluid environments in the TMOS sol. Data from Geddes *et al.* [25].

Figure 28A shows an anisotropy decay curve we have recorded for silica particle rotation in this colloidal suspension. As can be seen from Fig. 28A, an initially rapid depolarization is followed by a slower component. The slower anisotropy decay component (~400 ns) reflects the Brownian rotation of the colloidal particle, but the origin of the faster component (~5 ns) is unclear, although we do have a possible explanation. Wobbling of dye molecules tethered to the particle seems unlikely because 5 ns seems too long in the microviscosity of water [17,18]. Energy migration between dye aggregates on the particle and intramolecular reorientation of the emission dipole can be excluded on similar grounds. Figure 28B shows the $\chi^2$ analysis of the anisotropy data given in 28A (+) and synthetic data (O) generated for a normal distribution of mean radius 7.2 ± 0.1 nm solid silica particles undergoing Brownian rotational diffusion. In the analysis of the real data (+), the weaker and shorter correlation time of ≈5ns was allowed to vary freely, whereas the longer and dominating component, ≈95%, was fixed at different values corresponding to different particle size estimates during the least squares minimization of the $\chi^2$. As can be seen from Fig. 28B, the broader $\chi^2$ surface for the real data compared to the synthetic data implies that a distribution of particle sizes is present, although this appears relatively narrow. The skewness suggests the size distribution is weighted toward a mean radius >7.2 nm, where the colloid maybe in fact slowly aggregating with time. Interestingly, the shorter ≈5-ns component may in fact be a fitting artefact caused by the presence of a distribution of colloid sizes.

## CLOSING REMARKS

In this review article we have illustrated the potential that fluorescence has to offer for resolving the complex sol-gel formation kinetics for the many sol-gel systems. Although many workers have studied the sol to gel transition, few have considered the kinetics of particle formation and therefore haven't linked sol silica particles to gel parameters such as $t_g$ or other bulk properties such as syneresis. By labeling the growing (aggregating) silica nanometre-sized particles with a suitable fluorescent

**Table IV.** Silica Particle Radii Determined Using 1- (400 and 370 nm) and 2- 800 nm) Photon Excitation (The manufacturer's Radius Value for Ludox AM30 is 6 nm

| | Fluorescence decay parameters | | | | Anisotropy decay parameters | | | | |
|---|---|---|---|---|---|---|---|---|---|
| Sample | $\lambda_{exc}$ (nm) | $\tau_1$, $\tau_2$ (ns) | % | $\chi^2$ | $R_0$ | $\tau_r$ (ns) | % | $\chi^2$ | Particle radius (nm) |
| AM30 | 800 | 12.6 ± 1.20 | 21 | | 0.219 | 375 ± 90 | 90 | | 7.13 |
| | | 31.5 ± 0.63 | 79 | 1.18 | | 5.0 ± 4.8 | 10 | 1.11 | |
| AM30 | 400 | 14.0 ± 0.80 | 14 | | 0.276 | 431 ± 84 | 95 | | 7.47 |
| | | 33.6 ± 0.78 | 86 | 1.16 | | 4.2 ± 10.0 | 5 | 1.02 | |
| AM30 | 370 | 8.5 ± 0.12 | 41 | | 0.250 | 434 ± 69 | 100 | 1.09 | 7.48 |
| | | 25.4 ± 0.14 | 59 | 1.2 | | | | | |

A microviscosity of $10^{-3}$ PaS was used in the particle radii determination. For femtosecond 2-photon 800 nm, frequency doubled 800 nm to 400 nm and 370 nm IBH NanoLED nanosecond excitation, the channel width was ≈ 191 ps.

probe we have been able to observe and model a bulk property of sol-gels, now found at the particle level, namely syneresis. Based on this finding, it is therefore likely that the growth rates shown in our work, and those for others based on scattering techniques, are actually larger because of an offset by the intraparticle syneresis rate.

We believe our new interpretation and therefore approach to studying sol-gel glasses sets the scene for more complex sol-gel formation studies. For, example, although not stressed too much in this article, everything we have reported to date, even the static Ludox colloidal silicas, probably concerns a distribution of particle sizes, where for each size a different rate equation pertains. Our approach measures the mean particle size, where a distribution is likely to influence the overall reaction rates and therefore the physical characteristics of the final gels, such as pore size, given that pores are simply the voids between aggregated particles. Our studies also show that 1 and 2-photon time-resolved fluorescence anisotropy are ideal for studying many sol-gel kinetic processes that can occur simultaneously, such as hydrolysis, condensation, monomer addition, particle aggregation, and syneresis.

Other notable features of our approach are the resolution of the silica particle sizes, the cost as compared to neutron scattering, and the fact that this technique can be used at high silicate concentrations and well beyond $t_g$. This approach could easily be adapted for on-line

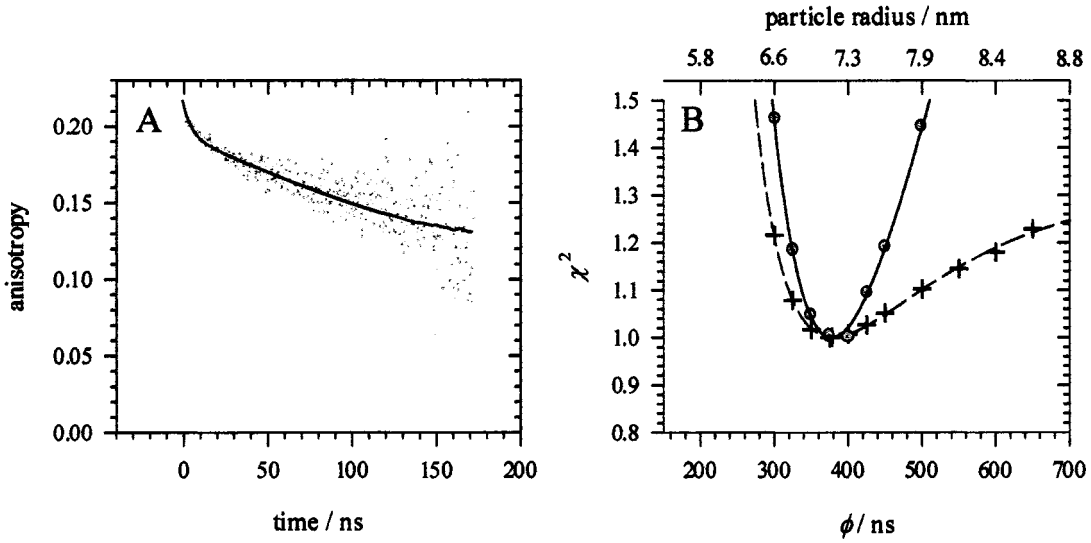


**Fig. 28.** A-Two-photon induced fluorescence anisotropy decay of Ludox AM30 particles labeled with CG437 ($\lambda_{ex}$ = 800 nm). The number of counts in the difference curve, i.e., numerator in Eq. (9), is ≈50,000 and the time per channel is 0.1927 ns. B-$\chi^2$ analysis of the anisotropy data given in A (+) and synthetic data (O) generated for a normal distribution of 7.2 ± 0.1 nm particles undergoing Brownian rotational diffusion. The minimum of the $\chi^2$ curve has been normalized to unity for comparison. Particle sizes are calculated assuming a microviscosity of 0.001 PaS. Data from Karolin *et al.* [23].

monitoring of sol-gel production in a manufacturing plant and should also be suitable for studying other colloids such as $TiO_2$, etc. In a more general context, this interpretation [Eq. (10)] also provides a means of separating the behavior of both free and bound dye. This may well offer a general approach to the problem of monitoring adsorption in related areas, for example, haze forming protein up-take by silica particles used in fining applications.

From a theoretical sol-gel formation perspective, much effort has been applied to solutions of Smoluchowski's equation and computer simulations, in the last few decades, to model silica cluster growth [1,2]. Reaction or diffusion-limited cluster-cluster aggregation (RLCA or DLCA) models [37], modified to take account of deformation as a result of rearrangement about the point of initial contact between clusters [38], have been considered successful at describing the kinetic and structural processes prior to gelation. At pH $<2$ the slightly positive repulsion between particles, which bind on collision according to the probability of an interparticle condensation reaction is thought to lead to RLCA conditions, which predicts growth [1,2] for non-gelling systems described by a mean diameter $r \sim e^{kt}$ (DLCA predicts $r \sim t$). It is therefore interesting that our experimental data, conversely supports low pH growth in the form $r \sim 1\text{-}e^{-kt}$, for sodium silicate–based hydrogels and $r \sim kt$ for a pH 2.3 TMOS gel. Also, current models do not take account of the intraparticle syneresis rate when modeling silica nanoparticle growth.

As we can see, fluorescence nanometrology in sol-gels is only just beginning, but our work already looks promising for experimentally determining the full kinetic and structural evolution of sol-gel glasses. This may in turn lead to a closer chemical control of the sol-gel process with outcomes potentially spanning a whole new generation of self assembled sol-gel materials with specified surface area's and pore sizes.

## ACKNOWLEDGMENTS

The author would like to thank John Revie at the University of Strathclyde for technical help with the fabrication of the sol-gel preparation rig, and John Broadfoot for electrical related work. The comments of Ineos Silica's, formerly Crosfield Chemicals and those of David Ward, (Unilever, UK) are also gratefully acknowledged. The work in this review article was undertaken at the University of Strathclyde, Glasgow, UK, with co-workers D.J.S. Birch and J. Karolin, and supported by the Engineering Physical Sciences Research Council (EPSRC), UK.

## GLOSSARY OF ACRONYMS AND MATHEMATICAL TERMS

| | |
|---|---|
| **c** | Rate of dye take-up Eq. (28) |
| **DLCA** | Difffusion limited cluster aggregation |
| **f** | Fraction of fluorescence due to bound dye |
| $\mathbf{f_0}$ | Initial fraction of fluorescence due to bound dye |
| $\mathbf{f_{max}}$ | Maximum fraction of fluorescence due to bound dye |
| **FD** | Frequency domain |
| **k** | Boltzmann constant and rate of primary particle aggregation for acidic sols |
| $\mathbf{k_p}$ | Rate of primary particle aggregation for alkaline sols |
| $\mathbf{k_s}$ | Rate of secondary particle aggregation for alkaline sols |
| **LD** | Laser diode |
| $\boldsymbol{\eta_b}$ | Bulk viscosity |
| $\boldsymbol{\eta_1}$ | Microviscosity calculated from $\tau_{r1}$ |
| **pt** | Polymerization time |
| **R6G** | Rhodamine 6G |
| **RET** | Resonance energy transfer |
| **r** | Silica particle radius |
| **R** | $H_2O$:Si ratio for TMOS sols, steady-state anisotropy, and linear regression coefficient |
| **RLCA** | Reaction limited cluster aggregation |
| $\mathbf{R_0}$ | Initial anisotropy |
| $\mathbf{r_0}$ | Initial silica particle radius |
| $\mathbf{r_p}$ | Primary silica particle radius for alkaline sols |
| $\mathbf{r_s}$ | Secondary silica particle radius for alkaline sols |
| $\mathbf{R_\infty}$ | Limiting anisotropy |
| $\mathbf{r_{max}}$ | Maximum particle radius |
| **SG** | Specific gravity |
| **TCSPC** | Time-correlated single-photon counting |
| **TD** | Time domain |
| **TEOS** | Tetraethylorthosilicate |
| **TMOS** | Tetramethylorthosilicate |
| $\mathbf{t_g}$ | Sol gelation time |
| $\boldsymbol{\tau_{r1}}$ | Free dye rotational correlation time Eq. (10) |
| $\boldsymbol{\tau_{r2}}$ | Bound dye rotational correlation time, Eq. (10) |

## REFERENCES

1. C. J. Brinker and G. Scherer (1989) *Sol-Gel Science: The Physics and Chemistry of Sol-Gel Processing*, Acad. Press, San Diego.

2. R. K. Iler (1979) *The Chemistry of Silica*, John Wiley and Sons Inc, New York.
3. A. H. Boonstra, T. P. M. Meeuwsen, J. M. E. Baken, and G. V. A. Aben (1989) A two-step silica sol-gel process investigated with static and dynamic light-scattering measurements, *J. Non-Cryst. Solids*, **109**, 153–163.
4. B. Himmel, Th. Gerber, and H. Burger (1987) X-ray diffraction investigations of silica-gel structures, *J. Non-Cryst. Solids* **91**, 122–136.
5. G. Orcel L. L. Hench, I. Artaki, J. Jonas, T, and W. Zerda (1988) Effect of formamide additive on the chemistry of silica sol gels 2. Gel structure, *J. Non-Cryst. Solids* **105**, 223–231.
6. R. Winter, D. W. Hua, P. Thiyagarajan, and J. Jonas (1989) A SANS study of the effect of catalyst on the growth-process of silica-gels, *J. Non-Cryst. Solids* **108**, 137–142.
7. N. L. Thompson (1991) *Fluorescence Correlation Spectroscopy: in Topics in Fluorescence Spectroscopy*, Vol. 1. *Techniques*, J. R. Lakowicz (Ed.) New York, Plenum pp. 337–410.
8. J. J. Birmingham, N. P. Hughes, and R. Treloar (1995) Diffusion and binding measurements within oral biofilms using fluorescence photobleaching recovery methods, *Phil. Trans. Royal Soc. Lon. B Bio. Sci.*, **350**, 325–343.
9. J. R. Lakowicz (1999) *Principles of Fluorescence Specroscopy*, 2nd ed., New York, Plenum.
10. B. Dunn and J. I. Zink (1997) Probes of pore environment and molecule-matrix interactions in sol-gel materials, *J. Chem. Mater.* **9**, 2280–2291.
11. R. Winter, D. W. Hua, X. Song, W. Mantulin, and J. Jonas (1990) Structural and dynamic properties of the sol-gel transition, *J. Phys. Chem.* **94**, 2706–2713.
12. B. Dunn and J. I. Zink (1991) Optical-properties of sol-gel glasses doped with organic-molecules, *J. Mater. Chem.* **1**, 903–913.
13. U. Narang, R. Wang, P. N. Prasad, and F. V. Bright, (1994) Effects of aging on the dynamics of Rhodamine-6G in Tetramethyl orthosilicate-derived sol-gels, *J. Phys. Chem.* **98**, 17–22.
14. G. D. Qian and M. Q. Wang (1999) Study on the microstructural evolution of silica gel during sol-gel gel-glass conversions using the fluorescence polarization of rhodamine B, *J. Phys. D. Appl. Phys.* **32**, 2462–2466.
15. C. D. Geddes, D. J. S. Birch, K. Apperson, J. M. Chevers, and I. McKeown (1999) Application of fluorescence depolarisation to dye uptake and particle sizing in silica sols, *SPIE Proc.* **3602**, 75–84.
16. C. D. Geddes, J. M. Chevers, and D. J. S. Birch (1999) Probing the sol-gel transition in $SiO_2$ hydrogels—A new application of near Infrared fluorescence, *J. Fluoresc.* **9**, 73–80.
17. C. D. Geddes and D. J. S. Birch (2000) Nanometre resolution of silica hydrogel formation using time-resolved fluorescence anisotropy, *J. Non-Cryst. Solids* **270**, 191–204.
18. D. J. S. Birch and C. D. Geddes (2000) Sol-gel particle growth studied using fluorescence anisotropy: An alternative to scattering techniques, *Phys. Rev. E.* **62**, 2977–2980.
19. D. J. S. Birch and C. D. Geddes (2000) Cluster Dynamics, Growth and Syneresis during Silica Hydrogel Polymerisation (2000), *Chem. Phys. Letts.* **320**, 229–236.
20. D. J. S. Birch and C. D. Geddes (2000) Fluorescence metrology of silica sol-gels: The effect of $D_2O$ and Inorganic salts, *P. Indian AS-Chem. Sci.* **112**, 311–322.
21. D. J. S. Birch, C. D. Geddes, J. Karolin, and K. Wynne (2001) Multiphoton excited fluorescence particle metrology: Application to silica hydrogels, *SPIE Proc.* **4252**, 97–103.
22. C. D. Geddes, K. Apperson, and D. J. S. Birch (2000) New fluorescent Quinolinium dyes—Applications in nanometre particle sizing, *Dyes Pigments* **44**, 69–74.
23. J. Karolin, C. D. Geddes, K. Wynne, and D. J. S. Birch (2002) Nanoparticle metrology in sol-gels using multiphoton excited fluorescence anisotropy decay, *Meas. Sci. Technol.* **13**, 21–27.
24. C. D. Geddes, J. Karolin, and D. J. S. Birch (2002) Sol-gel nanometrology: Gated sampling can reveal initial sol formation kinetics, *J. Fluoresc.* **12**, 113–117.
25. C. D. Geddes, J. Karolin, and D. J. S. Birch (2002) 1 and 2-photon fluorescence anisotropy decay in silicon alkoxide sol-gels: Interpretation in terms of self-assembled nanoparticles, *J. Phys. Chem. B* **106**, 3835–3841.
26. C. D. Geddes, J. Karolin, and D. J. S. Birch (2002) Fluorescence anisotropy in sol-gels microviscosities or growing silica nanoparticles offering a new approach to sol-gel structure elucidation, *J. Fluoresc.* **12**, 135–137.
27. R. F. Steiner (1991) Fluorescence Anisotropy: Theory and Applications, in *Topics in Fluorescence Spectroscopy*, Vol. 2. Principles J. R. Lakowicz (Ed.) Plenum, New York, pp. 1–51.
28. I. Gryczynski, H. Malak, and J. R. Lakowicz (1995) 3-Photon induced fluorescence of 2,5-diphenyloxazole with a femtosecond Ti:sapphire laser, *Chem. Phys. Letts.* **245**, 30–35.
29. D. J. S. Birch and R. E. Imhof (1991) Time Domain Fluorescence Spectroscopy Using Time-Correlated Single-Photon Counting: in *Topics in Fluorescence Spectroscopy.* Vol 1. *Techniques*. J. R. Lakowicz (Ed.) Plenum, New York, pp. 1–95.
30. A. Volkmer, D. A. Hatrick, and D. J. S. Birch (1997) Time-resolved nonlinear fluorescence spectroscopy using femtosecond multiphoton excitation and single-photon timing detection, *Meas. Sci. Technol.* **8**, 1339–1349.
31. D. A. Hatrick (1997) *Fluorescence of Near Infrared Rhodamine Dyes*, Ph.D. Thesis, University of Strathclyde, Glasgow, Scotland UK.
32. D. J. S. Birch, C. D. Geddes, J. Karolin, R. Leishman, and O. J. Rolinski (2002) Fluorescence Nanometrology in Sol-Gels. in *Springer Series on Methods and Applications of Fluorescence* Spectroscopy, Vol. 2. (In Press)
33. Du Pont (1987) Ludox colloidal silica, properties, uses, storage and handling, Data sheets.
34. A. VanBlaaderen and A. Vrij (1992) Synthesis and characterisation of colloidal dispersions of fluorescent, monodisperse silica spheres, *Langmuir* **8**, 2921–2931.
35. C. D. Geddes and D. J. S. Birch (2003) Sol-gel nanometrology in >pH 2 sol-gels, *J. Non-Cryst. Solids.* (In preparation.)
36. T. H. Gerber, B. Himmel, and C. Hubert (1994) WAXS and SAXS investigation of structure formation of gels from sodium-water glass, *J. Non-Cryst. Solids* **175**, 160–168.
37. P. Meakin (1983) *Phys. Rev. Letts.* **51**, 1119.
38. R. Jullien and A. Hasmy (1995) Fluctuating bond aggregation. A model for chemical gel formation, *Phys. Rev. Letts.*, **74**, 4003–4006.